Strong Shock Waves in Highly Porous Materials

by

Patrick X. Belancourt

A dissertation submitted in partial fulfillment
of the requirements for the degree of
Doctor of Philosophy
(Atmospheric, Oceanic and Space Sciences)
in The University of Michigan
2019

Doctoral Committee:

Professor R Paul Drake, Co-Chair
Dr. Paul A. Keiter, Los Alamos National Laboratory, Co-Chair
Associate Research Professor Carolyn C. Kuranz
Associate Professor Ryan D. McBride
Professor James A. Slavin

Patrick X. Belancourt

pxb@umich.edu

ORCID iD: 0000-0001-5807-1424

ACKNOWLEDGEMENTS

There are many people who have greatly supported me during my PhD work. First I would like to thank my advisors Paul Drake and Paul Keiter. Their support, feedback, and encouragement contributed to an enjoyable graduate school experience. I would also like to thank Carolyn Kuranz for not only initially introducing me to the group, but also for being a great mentor. Additionally, I would like to thank Wolfgang Theobald for teaching me how to do experiments on OMEGA EP. I would also like to thank Jim Slavin for gently introducing me to space science, and to Ryan McBride for being very accommodating on short notice.

I have made many wonderful friends during my graduate school studies. A special thanks to my grad school roommates, Sam Kishinevsky and Aaron Stein, as well as Zach Abbott, Ian Beil, Josh Davis, Laura Elgin, Jeff Fein, Greg Ledva, Heath LeFevre, Mike Macdonald, Alex Rasmus, and Hayley Warsinske. Thanks to the other graduate students in the group for the wonderful discussions, and thanks to Sallee Klein for the numerous hours spent driving to and from Rochester, NY, and for listening to podcasts with me.

I would especially like to thank my family, particularly my mom Linda, for all of their love and support through my numerous years of schooling. I am very grateful for my fiancé Cheryl for being extremely supportive and understanding, and introducing me to PA Dutch desserts.

Finally, I would like to thank the National Nuclear Security Agency and the Laboratory for Laser Energetics for supporting this work.

TABLE OF CONTENTS

LIST OF FIGURES

Figure

ABSTRACT

Strong shock waves traversing through porous materials occur in a broad range of applications. Foamed plastics are a popular material in many high-energy-density physics (HEDP) experiment due to the low, tunable density, and being easily machinable. Shocked foams are also of interest in equation of state (EOS) studies due to the ability to change the initial density to obtain different shocked states. Finally, the effect of porosity on asteroid collisions is needed to understand the cratering mechanism. This dissertation presents experimental and theoretical work related to strong shock waves in highly porous materials.

A platform to study shocked foams on the OMEGA EP laser system was developed in the first of a series of shot days. The imaging x-ray Thomson spectrometer (IXTS) was the main diagnostic and the measurement provided information on the compression, shock front location, temperature, and ionization, making it a potentially powerful diagnostic for equation of state measurements. The first shot day demonstrated the ability to perform the x-ray Thomson scattering technique on OMEGA EP. A second shot day improved the target design and obtained good quality data with a 150 mg/cc carbon foam. The experimental data was compared to Rankine-Hugoniot calculations of commonly used carbon EOS tables. The findings from this experiment suggest that the carbon EOS table over predicts the compression of the shocked carbon foam.

The theoretical aspect of this dissertation describes the pore closure in highly porous materials due to a strong shock wave. Many previous models of pore collapse

due to shock waves are in the low-pressure regime where the pore is crushed as a response to the shock wave. This dissertation presents a simple 1-D pore heating model where thermal radiation from the shock can penetrate deep into the porous material and cause heating of the pore walls. As the pore walls heat up, they start to expand and fill in the pores. This work suggests that there may be enough time for the pores to close prior to the arrival of the shock in conditions of interest to HEDP experiments.

CHAPTER I

Introduction

Porous materials have been researched and utilized throughout human history. The prominence of porous materials in ancient mythologies, such as the birth of the Greek Aphrodite from sea foam [37] and the birth of the Hindu Lakshmi from the foam of ocean milk [78], suggests that porous materials were well known in early human history. More tangible examples of porous materials in early human history would have been food, such as bread [65, 96] and beer foam [67, 3, 26], and cork, which was used for everything from flotation [21] to sealing containers [32]. Advances in optics allowed scientists to study porous materials rigorously, coinciding with Hooke coining the term cell from looking at cork under a microscope [42]. A drawing of the cells Hooke observed is shown in Figure 1.1 A). Scientist would also discover that objects in outer space could be porous, by studying meteorites [20] and the measurement of asteroid densities by spacecraft missions [12]. Advances in manufacturing have increased the present day popularity and porous material research, from everyday materials such as coffee cups and cushions [31], to ultra-low density aerogels [13]. Figure 1.1 B) shows the structure of a carbon nanotube aerogel, an example of an ultra-low density aerogel.

Percy Bridgman pioneered the study of materials at high pressures in the early 1900s. Bridgman created a device that could statically compress materials to around

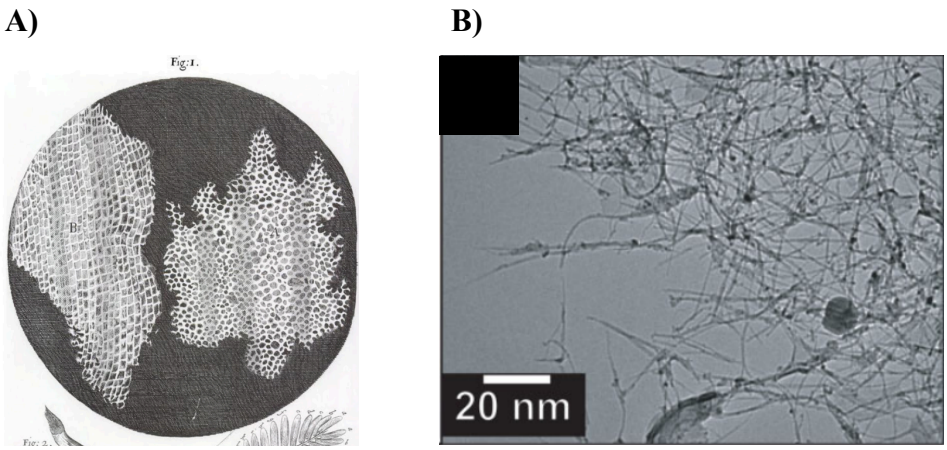

Figure 1.1: Examples of porous materials A) A drawing by Hooke of cells within a slice of cork (adapted from Hooke[42]. B) Example of a carbon nanotube foam, adapted from Bryning[13].

0.1 Mbar [11, 47], and was awarded the Nobel Prize in Physics in 1946 for this work. In the late 1950s the diamond anvil cell (DAC) [98, 46] was invented, allowing materials to be statically compressed to around one megabar. The DAC is still routinely used for statically compressed measurements and for precompression in dynamic experiments [48].

Shockwaves are used to dynamically compress materials to achieve pressures greater than 1 Mbar. While shockwave research was being conducted with gas in the 1800s, shock compression of solids intensified during and after the Second World War [54]. Chemical explosives were first used to reach pressures of a few hundred kilobars [4, 79, 63]. After the war, nuclear weapons were occasionally used to drive shocks with pressures of tens to hundreds of megabars [74, 75, 89, 90]. In recent years, large laser facilities such as the National Ignition Facility [39], Laser Megajoule facility [2], OMEGA laser facility [10] and others have been used to drive shocks ranging from one megabar to designs exceeding one gigabar [69, 85].

The convergence of shockwave research and aerogel breakthroughs have lead to porous materials being used in shock experiments. Foamed plastics in particular are routinely used in laser-driven shockwave research, discussed further in the next

subsection. Unfortunately, these experiments are often difficult to simulate with hydrodynamic models. It is often acknowledged that material properties, such as equation of state, are poorly known for shocked porous materials and the heterogeneous nature can be difficult to model. This dissertation presents theoretical and experimental work related to shocks traveling through highly porous materials. The theoretical work presents a simple 1-D model that shows void closure is possible due to heating of the upstream pore walls from thermal radiation of the shocked material. The experimental work compares the inferred density and temperature of shocked carbon foams to tabular equation of state tables commonly used in simulations.

1.1 Porous Materials in Extreme Conditions

Strongly shocked porous materials can have extreme material properties compared to thermodynamic conditions that are experienced normally on Earth. Shocked foams in particular can be compressed to near solid densities, with temperatures of tens to hundreds of eV. This regime is within the domain of high-energy-density physics (HEDP), which corresponds to pressures over 1 Mbar.

In this subsection I present a broad, but not exhaustive, summary of research topics involving shocked porous materials. The first part highlights research in laser-shocked foams, including hydrodynamic instability studies and equation of state measurements. The next part involves the proposed uses of foams in the inertial confinement fusion program. The third part introduces stockpile stewardship and the roles foam may have in nuclear weapons. The last part discusses the impact of porosity on asteroid collisions.

1.1.1 High-Energy-Density Physics

Foams are popular in HEDP experiments because they have a tunable density up to a couple orders of magnitude bellow solid density, and are easily machinable.

These attributes have contributed to foam being used in hydrodynamic instability experiments where a density mismatch and a well-defined initial perturbation between two fluids are often desired. For example, many experiments have used carbon foams to produce the Kelvin-Helmholtz instability in HEDP conditions [38, 95, 24]. Carbon [55, 86] and silica [77] foams have also been used in Rayleigh-Taylor instability work.

Foams with tunable densities offer the potential to measure different thermodynamic states that could not be achieved with a non-porous material and a single shock wave. EOS tables, which are often used in hydrodynamic simulations, use theoretical models that are tuned with experimental data and simulations. These EOS tables are typically not constructed with experimental data from shocked foam experiments due to a lack shocked foam data. Experiments are needed to determine the reliability and tune the models used in these tables in this regime.

Early foam EOS experiments used an aluminum EOS standard and the impedance mismatch technique to measure the shock velocity and particle velocity for optically transparent plastic foam [52]. Further work with optically transparent foams used the VISAR technique [17] to measure the shock velocity, particle velocity and density in a plastic [53] and silica [27] foam. More recently x-ray diagnostics have been used to probe foams that are opaque to optical light. This has included x-ray radiography to measure the shock position and density in carbon [1] and plastic [57] foams. X-ray Thomson scattering has also been used to measure temperature, density and ionization in carbon foams [28]. Finally, X-ray fluorescence has been used with titanium doped silica foam to infer the shocked density and temperature [59].

1.1.2 Inertial Confinement Fusion

An applied and actively researched area of HEDP is inertial confinement fusion (ICF), which is a subfield of fusion research. The broad goal of all fusion research is to demonstrate the feasibility of attaining net energy from fusion. The predomi-

nant method is to heat a Deuterium-Tritium (D-T) plasma to a few to tens of keV temperatures to fuse the deuterium and tritium. The fusion reaction,

$$\mathrm{D} + \mathrm{T} \longrightarrow {}^{4}_{2}\mathrm{He}(3.5\mathrm{MeV}) + \mathrm{n}(14.1\mathrm{MeV}) \tag{1.1}$$

releases kinetic energy in the form of a neutron designated as n above, and a ${}^{4}_{2}$He particle, which is often referred to as an α-particle. The kinetic energy of each particle is included in parenthesis above. The kinetic energy from the α-particle is envisioned to generate the heat that will drive power plants.

Broadly, there are two main approaches in fusion power research, magnetic confinement fusion and inertial confinement fusion (ICF), which differ on the approach of how to contain extremely hot plasma. In magnetically confined fusion,the low density and high temperature plasma is contained by strong magnetic fields. ICF on the other hand involves compressing the plasma to a thousand times solid density and then igniting it.

The main approach to laser driven ICF is termed hotspot ignition, which requires only a small volume to be hot enough for fusion. The energy released in the form of the α-particle heats up the neighboring volumes to drive further fusion reactions throughout the fuel. There are two main approaches to laser driven ICF [8], direct [15, 76] and indirect drive [64, 51], however the physics of the implosion is similar. A fuel target is irradiated with a drive energy, causing the implosion. In direct drive, this drive energy is from a number of lasers focused uniformly onto the ablator. In indirect drive, the lasers irradiate a hohlraum, which is typically gold. The hohlruam heats up and emits x-rays, which is used to drive the implosion.

A typical fuel target has two primary layers. The outer layer is an ablator and the inner layer is composed of frozen D-T fuel. The rest of the volume in the middle is D-T gas. The drive energy causes the outer layer to ablate, creating a spherical rocket

imploding inwards. The frozen D-T layer is compressed and the D-T gas reaches keV temperatures. The inertia from the compressed D-T layer keeps the hotspot contained long enough for the hotspot to fuse. In the ideal case, the α-particle from the fusion reaction deposits its energy into the cold, compressed layer, causing heating and conditions for fusion. This in turn will create more energetic α-particles, which will be deposited in a section further into the fuel. In summary, the hotspot contains the initial fusion reaction, and then the alpha particles create a bootstrapped fusion wave in the compressed fuel.

Foams have been proposed in the design of ICF targets for both direct and indirect drive ICF. In direct drive, foams have mainly been considered as an ablator to reduce the affects of laser imprinting [68, 97, 45]. Laser imprinting refers to the variance in the spatial and temporal laser drive seeding instabilities such as Rayleigh-Taylor instability. A low density foam ablator would lower the Rayleigh-Taylor growth rate by increasing the ablation velocity, mitigating the instability.

In indirect drive, foams have been proposed to line hohlrums and as a layer in the fuel target. The hohlrum is heated with lasers to produce x-rays to drive the compression of the fuel target. This heating causes expansion, which interferes with the lasers, leading to asymmetrical implosions. Lining the hohlrum with foam is envisioned to slow the expansion, leading to more uniform compression of the fuel target [9]. The second aspect is using a wetted foam instead of a frozen D-T layer [70, 102]. The foam would serve as a matrix to hold liquid D-T. The initial temperature of the fuel target can be varied to change the vapor pressure of the D-T gas in the middle of the target.

1.1.3 Stockpile Stewardship

Underground nuclear weapon testing was used to test variations and components of nuclear weapon design. In 1992, President George H.W. Bush ended underground

testing, leading to science based stockpile stewardship (SBSS) [22, 71]. The goal of SBSS is to maintain the nuclear deterrent by ensuring the integrity of current nuclear weapons and by maintaining expertise in weapon physics. Large experimental facilities, such as the National Ignition Facility, have been built to study the physics pertaining to nuclear weapons in an isolated or integrated manner. Large supercomputers have been commissioned in parallel with the experimental facilities. Experimental data can be used to refine material properties in radiation hydrodynamics codes, such as the equation of state and opacity, or to benchmark the accuracy of radiation hydrodynamics codes in reproducing the integrated experiments.

Assessing the role that foams play in SBSS in difficult due to the classified nature of the program. A Lawrence Livermore National Laboratory whitepaper [71] mentions foams in a few places, mainly for use in radiation hydrodynamic experiments. An additional potential case is the material codenamed Fogbank, which is used in W76 nuclear warheads from the 1980s [72]. Fogbank is rumored to be an aerogel foam that separates the two stages of a fusion nuclear weapon. When the W76 warhead was refurbished starting in 2007, it was discovered that the United States lost the ability to manufacture Fogbank due to closing of the manufacturing facility and the retirement of the workers [92]. A substitute material was considered, but the impact of changing the materials could not be determined with simulations. In total, around $100 million was spent to reproduce Fogbank [91].

1.1.4 Asteroid Collisions

Asteroids can be porous materials due to having micropores and macropores. Micropores are the typical voids in a porous material. Macropores arise when asteroids are composed of many rocks that are gravitationally held together, which is termed a ruble pile [94]. The affects of porosity on asteroid impacts have recently been studied due to cratering mechanisms and the related deflection of asteroids.

In 1997, the Near Earth Asteroid Rendezvous (NEAR) spacecraft flew to the asteroid Mathilde [93]. The NEAR spacecraft observed craters that were unusually shaped and isolated from one another. A laboratory experiment [44, 43] found that the cratering mechanism is different for porous materials. Typical cratering is due to the ejection of material from an impact. For porous materials, the cratering occurs from the compaction of the voids. This compaction absorbs energy and attenuates the shock from disturbing nearby craters.

Relatedly, there is ongoing research determine the feasibility of deflecting an asteroid that is headed for Earth. The two main methods proposed for deflecting an asteroid are with nuclear weapons [87] or kinetic impactors [88]. The porosity affects the deflection in two somewhat opposing ways. First, as described in the paragraph above, energy from the impact goes into crushing the pores, leaving a reduced energy for deflection. Second, for asteroids of similar sizes, high porosity asteroids have less mass than low porosity asteroids. Lower overall mass leads to less energy that is needed to change the momentum of an incoming asteroid. Studying the consequences of these two effects are important because only the size of a potential asteroid may be known.

1.2 Description of Porous Materials

Porous materials are materials with pores that can be filled with another substance, such as a gas, a liquid, or vacuum. The terminology this thesis will use is that voids refer to the special case of empty pores. The result of the pores is a material with an average density that is less than the solid density of the same material. A common classification for porous materials is the porosity ϕ, which is the ratio of the volume of the voids V_V to the total volume of the porous material V_T, given as

$$\phi = \frac{V_V}{V_T}. \tag{1.2}$$

Related parameters that are often used in porous material theory are the relative density RD, and the distention parameter α. The relative density is defined as the ratio of the average density of porous material ρ_{pm} to the density of the solid material without pores, ρ_s given by $RD = \rho_{pm}/\rho_s$. The distention parameter is the reciprocal of the relative density, $\alpha = 1/RD = \rho_s/\rho_{pm}$. The distention parameter will be used briefly in Chapter 2 to describe pore crushing models. The relative density has been classically used to describe the mechanical properties of porous materials, and is included here for context. With minor algebra, the porosity can be related to the distention parameter and the relative density as given below.

$$\phi = \frac{V_V}{V_T} = 1 - \frac{\rho_{pm}}{\rho_s} = 1 - \frac{1}{\alpha} = 1 - RD. \tag{1.3}$$

Porous materials are interesting and challenging due to the variety of scale lengths present. On the macroscopic scale, the average density and the porosity characterize the porous material. The properties of the pore walls are important on the microscopic scale, where the pore wall widths can be as small as tens of nanometers. The mesoscale encompasses features in between microscale and macroscale, such as potentially the size of the pores.

Porous materials can be classified as a closed-cell or open-cell. Closed-cell pores are pores that are totally surrounded by solid density material and isolated from other pores. Historically, closed-cell porous materials have been used for insulation and flotation. Open-cell porous materials have interconnected pores. Open-cell porous materials are common in geology, cushions and ultra-low density foams.

Gibson and Ashby have defined cellular solids to be porous materials that have porosities greater than about 0.7 [33]. This limit corresponds to the material being composed of mostly pores, as opposed to isolated cases such as defects. In this thesis, I will use this definition as the rough boundary for high porosity foams. The high porosity foams used in this work are open-celled and are used in a vacuum chamber.

Taking this scenario into account, the pores are considered empty, and the term voids is used interchangeably with pores.

1.3 Individual Contributions

This section acknowledges support by collaborators that helped make this dissertation work possible.

- **Chapters 1 and 2**: These chapters contain the accumulated knowledge of historical work and foundational science that pertains to shocked porous materials, and have been cited appropriately.

- **Chapter 3**: The initial experimental design was developed by Wolfgang Theobald at LLE and tweaked by myself. The targets were assembled at LLE, and Sallee Klein assisted with diagnostic support. All of the data analysis was done by myself, and was supervised by Paul Keiter and Wolfgang Theobald. Gianlucca Gregori wrote the code used to generate theoretical x-ray Thomson scattering spectra.

- **Chapter 4** The experimental target was based of the targets used in Chapter 4 (developed by Wolfgang Theobald), and was redesigned by myself. The targets were assembled at LLE, and Sallee Klein assisted with diagnostic support. Suxing Hu from LLE gave insight into EOS tables and theory. All of the data analysis was done by myself, and was supervised by Paul Keiter and Wolfgang Theobald. Gianlucca Gregori wrote the code used to generate theoretical x-ray Thomson scattering spectra.

- **Chapter 5**: This chapter contains theoretical work was developed by myself with the feedback and guidance from Paul Drake.

1.4 Summary of Chapters

Chapter 2: This chapter contains background science that is fundamental to this dissertation. The first part of this chapter derives the jump conditions starting from the hydrodynamic conservation equations, derivation of the Hugoniot, discussion of equation of state, and models describing shock waves traveling through porous solids. The last section of this chapter will discuss important physics related to doing an experiment with laser-driven shock waves, including Laser ablation, x-ray production from a laser-heated foil, and x-ray Thomson scattering.

Chapter 3: This chapter describes the development of the imaging x-ray Thomson scattering technique on the OMEGA EP laser system, and was published in *Review of Scientific Instruments*.[6] The experimental geometry is discussed, and the data and analysis from the imaging x-ray Thomson spectrometer (IXTS) is presented.

Chapter 4: This chapter presents data and analysis of a shocked carbonized resorcinol-formaldehyde foam, using the basic platform developed in Chapter 4. Changes to the platform are noted, and thermodynamic parameters that are inferred from the IXTS is compared to commonly used equation of state tables.

Chapter 5: This chapter presents theory for void closure in shocked, high porosity material. The first part of the chapter introduces the 1-D heating model that was developed to estimate heating of pore walls due to thermal radiation from the shock. The next sections estimate pore closure and offer implications for equation of state and modeling of these systems.

Chapter 6: This chapter summarizes the dissertation work, and offers my thoughts on future work that could build off of this dissertation work.

CHAPTER II

Laser-Driven Shock Wave Physics

This chapter reviews the physics relevant for this dissertation work. In the first part of this chapter, I discuss the basic aspects of shock wave physics that are foundational to both the experimental and theoretical aspects of this dissertation. The second part of this chapter reviews the underlying physics of driving a shockwave at the OMEGA EP laser facility, and the x-ray Thomson scattering method used to diagnose the shocked material.

2.1 Shock Waves

A shock wave is a disturbance that travels faster than the speed of sound in a material. Examples of such systems include bow shocks diverting the supersonic solar wind about the planets [50], the sonic booms of fighter jets [82], and blast waves from nuclear explosions [56]. The structure of a shock wave has three main features, as indicated in Figure 1. The first feature is the material upstream of the shock wave, which is in the initial, unshocked state. The second feature is the downstream region, which has been heated and compressed by the shock wave. The third region is the shock front, which travels faster than the speed of sound into the upstream material, and separates the shocked and unshocked regions.

The behavior of the shock wave is analyzed with the Euler equations below, which

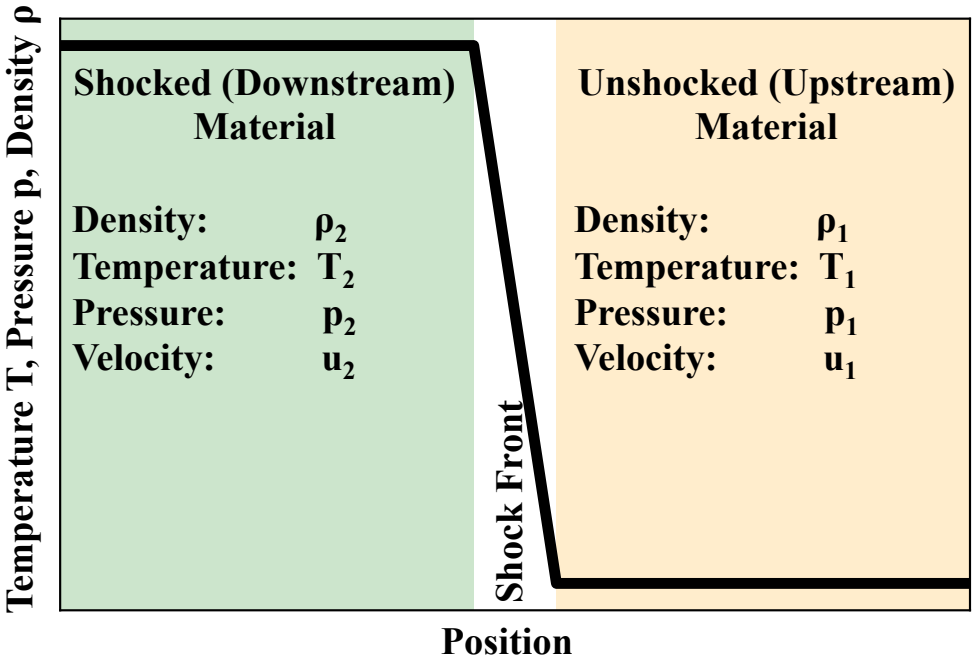

Figure 2.1: Schematic of a shock wave geometry. The shock wave is propagating through a material with initial conditions indicated with the subscript 1 and shaded orange. The shock acts to heat and compress the material, with conditions indicated with subscript 2 and shaded in green. The shock front travels at velocities greater than the speed of sound in the unsocked material, and separates the shocked and unshocked regions (shaded in white).

conserves mass, momentum and energy.

$$\frac{\partial \rho}{\partial t} + \nabla \cdot \rho \mathbf{u} = 0 \qquad \text{Conservation of Mass} \quad (2.1a)$$

$$\frac{\partial}{\partial t}(\rho \mathbf{u}) + \nabla \cdot (\rho \mathbf{u}\mathbf{u}) + \nabla p = 0 \qquad \text{Conservation of Momentum} \quad (2.1b)$$

$$\frac{\partial}{\partial t}\left(\frac{\rho u^2}{2} + \rho\epsilon\right) + \nabla \cdot \left(\rho \mathbf{u}\left(\epsilon + \frac{u^2}{2}\right) + p\mathbf{u}\right) = 0 \qquad \text{Conservation of Energy} \quad (2.1c)$$

Here ρ is the mass density, $\mathbf{u}$ is the velocity, p is the pressure and ϵ is the specific internal energy. I will follow the approach outlined in many textbooks [101, 25] by assuming that the shock front is a discontinuity and contains none of the material fluxes. With this assumption, the material fluxes upstream and downstream of the

discontinuity have to be equal and are given below.

$$\rho_1 u_1 = \rho_2 u_2 \qquad \text{Mass} \qquad (2.2a)$$

$$\rho_1 u_1^2 + p_1 = \rho_2 u_2^2 + p_2 \qquad \text{Momentum} \qquad (2.2b)$$

$$\rho_1 u_1 \left(\epsilon_1 + \frac{u_1^2}{2}\right) + p_1 u_1 = \rho_2 u_2 \left(\epsilon_2 + \frac{u_2^2}{2}\right) + p_2 u_2 \qquad \text{Energy} \qquad (2.2c)$$

Here subscript 1 designates material upstream of the shock front discontinuity and subscript 2 designates the downstream material. These equations are colloquially referred to as the Rankine-Hugoniot jump conditions. The jump conditions were derived implicitly in the frame of reference where the shock front is stationary. In laboratory settings, the shock front is typically traversing through a stationary upstream material. In this lab frame of reference, the shock front will have a velocity of $u_s = -u_1$, and the downstream velocity is $u_p = u_1 - u_2$.

The jump equations have eight variables between the three jump conditions, corresponding to density, velocity, pressure and internal energy in the shocked and unshocked maerial. Typically the unshocked material is well characterized and known, resulting in four unknown variables of the shocked material with three jump conditions. The result is specifying, or measuring, two of the shocked material variables determine the rest of the shocked material variables.

The jump conditions can be rearranged algebraically to present them in a form of $Y = H(X_1, X_2)$, where X_1, X_2 are the two of the shocked material parameters that are specified and Y is an unknown shock parameter of interest. These equations are referred to as the Hugoniot.

An example of a Hugoniot that is used in this work is given below. The shock velocity and shocked density was measured experimentally, and we were interested in determining the shocked pressure. The shocked pressure can be found by combining the mass and momentum jump conditions by eliminating the downstream velocity,

which was not measured.

$$p_2 - p_1 = u_1^2 \left(\rho_1 - \frac{\rho_1^2}{\rho_2} \right) \tag{2.3}$$

A very common Hugoniot that will be used in following sections can be found by combining all three jump conditions through eliminating u_1 and u_2, resulting in

$$\epsilon_2 - \epsilon_1 = \frac{1}{2} (p_2 + p_1) \left(\frac{1}{\rho_1} - \frac{1}{\rho_2} \right). \tag{2.4}$$

The Hugoniot does not define the path a material takes in going to the shocked state. Instead, the Hugoniot represents the collection of all possible states that can be achieved with a single shock in a material with a known initial state. The Hugoniot will be exploited in the upcoming sections as a method of measuring the equation of state of a material.

2.1.1 Equation of State

The conservation and jump equations are not complete, meaning that there are more variables to be solved for than equations. This scenario is known as the closure problem, and requires an additional equation, termed the equation of state (EOS), to solve the problem. The EOS conveys the material's unique properties by expressing the relationship between thermodynamic variables. Shock waves are a common tool to measure the EOS because the states that can be reached with a shock wave are constrained and given by the Hugoniot equations. An EOS must be explicitly provided to solve the conservation equations analytically or numerically. The following subsections describe two EOS, ideal gas EOS and tabular EOS, which are often used in high-energy-density physics.

2.1.1.1 Ideal Gas Equation of State

The ideal gas law for a system of electrons and ions for pressure and specific internal energy is

$$p = \frac{(1+Z)\rho k_B T}{A m_p} \tag{2.5}$$

and

$$\epsilon = \frac{n}{2}\frac{(1+Z)k_B T}{A m_p}. \tag{2.6}$$

Here n is the number of degrees of freedom, Z is the ionization, k_B is the Boltzmann constant, ρ is the mass density, T is the temperature and Am_p is the mass of the ions. A simple relationship between pressure and specific internal energy can be found by taking the ratio of specific internal energy and pressure, given as

$$\epsilon = \frac{n}{2}\frac{P}{\rho}. \tag{2.7}$$

The ratio of specific heats, or the adiabatic index is

$$\gamma = \frac{C_p}{C_V} = \frac{\frac{\partial \epsilon}{\partial T}\big|_p}{\frac{\partial \epsilon}{\partial T}\big|_V} = 1 + \frac{2}{n} \tag{2.8}$$

Where C_p is the specific heat at constant pressure and C_V is the specific heat at constant volume. Common values encountered for n and γ include n=2 (γ=2) for crystalline solids, n=3 (γ=5/3) for monoatomic gasses, and n=5 (γ=7/5) for diatomic gasses and radiating plasmas. Equation 2.7 can be plugged into Equation 2.8 to obtain

$$\epsilon = \frac{p}{\rho(\gamma - 1)}. \tag{2.9}$$

The behavior of shocks at high pressures can now be analyzed with an ideal gas EOS. Starting with the Hugoniot in Equation 2.4, we assume that the $p_2 \gg p_1$ and

$\epsilon_2 \gg \epsilon_1$, or $p_1 \approx 0$ and $\epsilon_1 \approx 0$. Inserting Equation 2.9 with these assumptions gives

$$\frac{p_2}{\rho_2(\gamma-1)} = \frac{p_2}{2}\left(\frac{1}{\rho_1} - \frac{1}{\rho_2}\right). \tag{2.10}$$

After some algebraic rearranging, Equation 2.10 becomes

$$\frac{\rho_2}{\rho_1} = \frac{\gamma+1}{\gamma-1}. \tag{2.11}$$

This is known as the strong shock limit ($p_2 \gg p_1$). Note that while the compression ρ_2/ρ_1 asymptotes with large shocked pressures, the temperature does not, as can be seen in Equation 2.5.

Equation 2.9 and Equation 2.5 can be used to solve the Hugoniot equation in Equation 2.4. The results of the calculation with three different initial temperatures, T= 0.0025 eV, 1 eV, 10 eV, an initial density of 150 mg/cc and γ=5/3 is shown in Figure 2.2. The general result is that for higher initial temperatures, the shocked material is at lower densities and higher temperatures, compared to lower initial temperatures at the same shocked pressure. This shows that changing the initial temperature can either be used as a method to access different states with pressures under the strong shock limit, or that unintentionally changing the initial temperature could lead to a different state than expected.

2.1.1.2 Tabular Equation of State

Equation of state tables [83, 58, 7] precompute complicated, computationally expensive, and disjoint models, and output the results to a lookup table that a hydrodynamics code can read. There are numerous advantageous with using an EOS table for a complex hydrodynamic simulations. EOS tables can straightforwardly incorporate a vast range of temperature and density space and use models and physics that are material specific in subsets of that phase space. EOS measurements, when available,

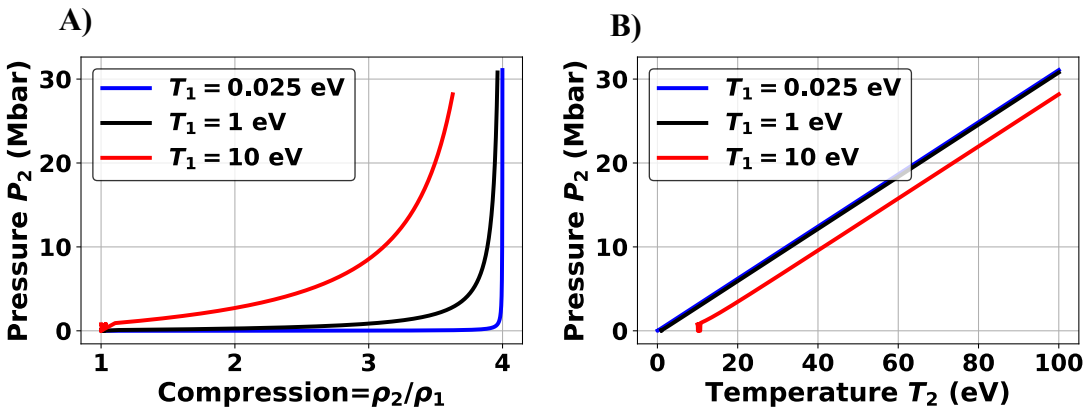

Figure 2.2: Solution of Hugoniot Equation 2.4 using an ideal gas EOS with Equation 2.9 and Equation 2.5. Calculations were performed with ρ_1=150 mg/cc, and $\gamma = 5/3$. Figure A) shows the compression decreases with increasing initial temperature T_1. Figure B) Shows that the shocked temperature T_2 increases with increasing initial temperature.

are often incorporated into EOS tables by tuning the models with the measurement. Since EOS tables are precomputed, the hydrodynamic code does not need to do any expensive EOS computation, and the tables can be shared with collaborators.

Caution must be taken when using EOS tables for shocked porous materials, however. EOS tables are often built for a specific problem, and that often does not include shocked foams. There is also very little experimental data available for most porous materials, which means the tables will not be tuned in this density and temperature space. Documentation for the EOS tables that covers issues such as what models were used, if any experimental data is included, and what assumptions went into the models, are often hard to come by due to the fact that most tables are built at national laboratories and the EOS tables can be decades old. Lastly, the concept of an EOS may not rigorously apply to shocked foams. Shocked foams differ from shocked gasses due to the presence of pores in foams that the shock wave encounters. These pores are crushed by a shock wave, causing an irreversible process that is inconsistent with an EOS treatment. Pore collapse models are discussed below, and offer a possible solution where the affects of pore crushing are separated from the

EOS.

2.1.2 Shocked Porous Materials

Porous materials are used in shock wave studies in part because the initial low-density allows access to states that are not achievable with a solid density sample. To explore this further, we use Equation 2.9 and Equation 2.5 to solve the Hugoniot equation in Equation 2.4. Here we set the initial temperature to room temperature $T_1 = 0.025$ eV and $\gamma = 5/3$. Three initial starting densities of ρ_1 =1 g/cc, 0.1 g/cc, 0.05 g/cc, corresponding to a typical solid density of most plastics, porosities of 0.9, and 0.95 respectfully, are used to show the dependence on initial density of the behavior. The results of the calculation are given in Figure 2.3. Figure 2.3 A) shows that the density reaches the strong shock limit in Equation 2.11 for each of the initial densities. The general trend is that with the same shock pressure, lower density material will reach lower shocked densities and higher shocked temperatures. These results show that changing the initial density in shock EOS studies is a good option to access density and temperature regimes that are not normally accessed with solid densities.

The above calculation makes no distinction between a homogeneous gas and heterogeneous foams with vacuum voids dispersed into a solid density matrix. Compaction models have been developed to describe the crushing behavior of the pores at low shock pressures. The P-α model [41, 16, 14, 60] is the most widely used compaction model, which models the change in the distention parameter $\alpha = \rho_s/\rho_p$, where ρ_s is the solid density of the material and ρ_p is the porous material density, as a function of pressure. The pressure of the porous material is given as

$$p_p = \frac{1}{\alpha} p_s \left(\frac{\rho_p}{\alpha}, \epsilon \right), \tag{2.12}$$

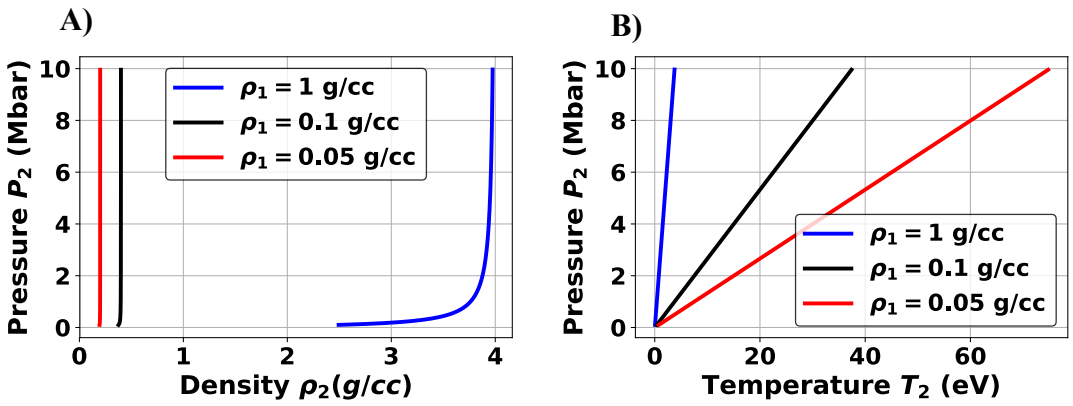

Figure 2.3: Solution of Hugoniot Equation 2.4 using an ideal gas EOS with Equation 2.9 and Equation 2.5. Calculations were performed with T_1=0.025 eV, and $\gamma = 5/3$. Figure A) shows the compression asymptotes to $\rho_2/\rho_1 = 4$, while Figure B) Shows that the shocked temperature T_2 increases with decreasing initial density.

where p_s is the pressure of the solid material, and ϵ is the internal energy of the porous material, which is assumed to be the same as the internal energy of the solid material. The distention parameter is given by a crush function, which is commonly expressed as have an elastic crushing part

$$\alpha(p_p) = \frac{p_p}{p_e}(\alpha_p - \alpha_e) + \alpha_e, \tag{2.13}$$

and a plastic crushing part

$$\alpha(p_p) = (\alpha_p - 1)\left(\frac{p_s - p_p}{p_s - p_e}\right)^2 + 1. \tag{2.14}$$

Here α_e is the elastic distention parameter and is the starting distention parameter, p_e is the pressure where plastic deformation occurs, α_p is the distention parameter where plastic deformation occurs,p_s is the pressure where the void is fully compacted. The pressure parameters are generally acquired through fitting to experimental data, but are often of order of tens of kilobars.

One of the main advantageous of the P-α model is that it relies on EOS of the

solid density material, as can be seen in Equation 2.12, which is usually better experimentally studied. Unfortunately the P-α model usually needs to be iteratively solved, since α_p and p_p both depend on each other.

2.2 Laser-Driven Shock Waves

This part of the chapter reviews the physics involved with experimentally producing and diagnosing laser-driven shock waves that are relevant for this dissertation .

2.2.1 OMEGA EP Laser Facility

The OMEGA EP laser system [62] is one of two laser systems at the Laboratory for Laser Energetics in Rochester, NY. The OMEGA EP laser system has 4 NIF-like, long-pulse beams with pulse lengths ranging from 100 picoseconds to 10 nanoseconds. The beams are frequency tripled to a wavelength of 351 nm, and each beam can have a maximum energy of 4.4 kJ. Distributed phase plates are available to give a super-Gaussian intensity profile with the diameter of the focal spot, also known as spot size, ranging from 400 microns to 2 mm. Two of the four beams can also be compressed to form a short pulse laser beam, however this feature was not used for this dissertation.

2.2.2 Laser Ablation

High power lasers can be used to generate strong shock waves into a material. For example, at the OMEGA EP laser facility, a 10 ns beam with 4.4 kJ of energy focused onto a 750 μm spot size results in around 400 GW of power and intensities around 1x10^{14} W/cm^2. The mechanism of generating high pressures to drive the shock wave is through heating of the material to few keV temperatures and having the plasma blow off to create a driving force into the material, similar to a rocket. This mechanism involves absorption of the laser light by the material, and then the

transport of the energy by electrons deeper into the material to sustain the pressure. This process is colloquially referred to as laser ablation.

The first step in laser ablation is the absorption of the laser energy by the plasma. At laser intensities in the regime of 1x10^{14} W/cm^2, the plasma extracts energy from the laser due to inverse Bremsstrahlung up to the critical density. The critical density is the point where the plasma totally reflects the laser light due to laser frequency being equal to the plasma frequency. The scaling of the critical density with the laser wavelength can be found by equating the laser frequency with the plasma frequency, given as

$$n_c = \frac{\omega_0^2 m_e \epsilon_0}{e^2} = 1.1\text{x}10^{21} \lambda_{\mu m}^{-2} \quad \text{cm}^{-3}. \tag{2.15}$$

Here n_c is the critical density expressed in units of cm^{-3}, ω_0 is the laser frequency, m_e is the mass of an electron, ϵ_0 is the vacuum permittivity, e is the charge of an electron, and $\lambda_{\mu m}$ is the wavelength of the laser in microns.

The second step in laser ablation is the transport of energy by the electrons from the critical density to deeper into the plasma. Following the framework by Drake [25], a flux limited, free-streaming heat flux model is used to describe the transport of electrons past the critical density. The free-streaming thermal electron flux, Q_{FS}, is

$$Q_{FS} = f n_c k_B T_e v_{th} = \frac{f n_c \left(k_B T_e\right)^{3/2}}{m_e^{1/2}}, \tag{2.16}$$

where f is a flux limiter that is tuned to take into account physics not included in the model, k_B is the Boltzmann constant, v_{th} is the electron thermal velocity, and T_e is the electron temperature. To obtain a scaling of the electron temperature, we will assume half of the laser intensity goes into producing the free-streaming thermal electron flux, or $0.5I = Q_{FS}$. Noting that I is the laser intensity and assuming

f=0.05, the electron temperature in keV is

$$T_e = 2.6 I_{14}^{2/3} \lambda_{\mu m}^{4/3} \quad \text{keV}. \tag{2.17}$$

Here I_{14} is the laser intensity in units of 1x10^{14} W/cm^2. The ablation pressure at the critical density is the plasma thermal pressure,

$$P_{abl} = P_{th} = \frac{n_c}{Z} (1 + Z) k_B T_e = 6.1 I_{14}^{2/3} \lambda_{\mu m}^{-2/3} \quad \text{Mbar}. \tag{2.18}$$

Here the ablation pressure P_{abl} is given in units of Mbar, Z is the ionization and (1+Z)/Z is approximated as 1. For the laser conditions for this work, $\lambda_{\mu m}$ =0.351 μm and I_{14}= 1x10^{14} W/cm^2, the ablation pressure is around 14 Mbar.

2.2.3 X-ray Probe Production

Often it is advantageous to probe a plasma with electromagnetic radiation to determine information about the state of the system. Optical laser light can be a poor probe for solid density plasmas due to the electron density being greater than the critical density for optical photons. Therefore it is often desirable to convert the laser light into x-ray photons.

The approach in this dissertation work is to convert laser light into characteristic line emission to use as an x-ray probe. The process for this conversion is in parallel to that of laser ablation. The laser irradiates a mid-Z foil, forming a blow-off plasma with temperatures of a few keV. For these conditions, the ions are highly ionized and a portion of the ions is in Helium-like electron configuration. A fraction of the electrons in this blow-off plasma have enough energy to excite an electron from the 1s state to the 2p state. A photon is emitted when the excited electron transitions back into the ground state, $1s^1 2p^1 \rightarrow 1s^2$. This photon has an energy that is equal to the difference between the energy of the two states, resulting in a narrow bandwidth x-ray

probe with photon energies of a few to around 10 keV, depending on the material.

Previous studies [99, 61, 5] show that the efficiency for converting laser energy into line emission peaks at laser intensities of around 1x10^{15} W/cm^2 for mid-Z foils. The peak conversion efficiency can be around 1% and falls off past intensities of 1x10^{16} W/cm^2. These findings motivated the decision to use three of the four OMEGA EP beams to generate the x-ray source, with combined total laser energy is 3.75 kJ with a pulse length of 1 ns and a spot size of 400 μm, resulting in an intensity of about 3x10^{15} W/cm^2.

2.2.4 X-ray Thomson Scattering

X-rays generated from laser-irradiated foils can be used to probe solid density plasmas. Radiography is a diagnostic technique that records the transmission of the x-rays through the plasma, resulting in a line-integrated density and shock front location measurement. X-ray Thomson Scattering (XRTS) on the other hand, measures the scattering of the x-ray probe, providing further information on the state of the plasma. The imaging x-ray Thomson spectrometer (IXTS), the main diagnostic used for this dissertation work, spectrally resolves the scattered x-ray probe, while imaging in 1-D. For the conditions in this work, inferences of the temperature and ionization are made by analyzing the scattered x-ray spectra, and a 1-D density profile is obtained from the spatially resolved imaging.

To highlight the power of measuring the scattering of the x-ray probe, I will first describe the scattering from a free election, with a schematic given in Figure 2.4. The scattering vector **k** is defined as the difference between the probe vector and the scattered vector. Assuming small momentum transfer to the electron, the magnitude of the scattering vector can be approximated as $k \approx 2k_0 \sin(\theta/2)$, where θ is the scattering angle. The change in frequency, ω, is given by

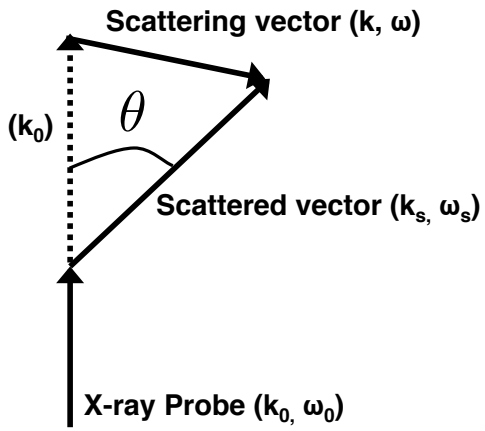

Figure 2.4: Schematic of x-ray scattering geometry. The initial x-ray probe, characterized by wave number k_0 and frequency ω_0 is scattered by an electron, with a resulting wave number k_s and frequency ω_s. The scattering vector represents the shift in wave number and frequency as a result of the scattering.

$$\omega = -\frac{\hbar k^2}{2m_e} \pm \mathbf{k} \cdot \mathbf{v}, \tag{2.19}$$

where $\hbar$ is the reduced Planck constant, m_e is the mass of an electron, and $\mathbf{v}$ is the velocity of an electron. The first term is Compton scattering and involves information only about the scattering geometry. The second term is Doppler broadening, which contains information about the plasma through the velocity component. For example, if the electron distribution is Maxwellian ($\mathbf{v} \propto \sqrt{T_e}$), then a temperature measurement can be obtained from the width of this Doppler broadening term.

For a collection of electrons, the x-ray probe scatters off of the fluctuations of the electrons in a plasma. The fluctuations occur in two regimes, depending on the scale length that is probed. For small scale lengths compared to the shielding length, the x-rays scatter from individual electrons. For longer scale lengths, the x-ray probe scatters from the electron plasma waves. The scattering parameter, $\alpha = \frac{1}{k\lambda_s}$, is used to quantify these two scattering regimes. Here λ_s is the shielding length, which for conditions in this dissertation can be taken as the Debye length, $\lambda_s = \sqrt{\frac{\epsilon_0 k_B T_e}{e^2 n_e}}$.

Here ϵ_0 is the vacuum permittivity, k_B is the Boltzmann constant, T_e is the electron temperature,e is the charge of an electron, and n_e is the electron density. For $\alpha > 1$, the scattering is in the collective regime, indicting that the measured scattered x-rays are from the electron plasma waves. For $\alpha < 1$, the x-ray probe scatters off of individual electrons, termed the non-collective regime. The work in this dissertation is all in the non-collective regime.

The power of the scattered x-ray probe [34], Ps, is given by

$$P_s d\Omega d\omega = \frac{P_0 r_0^2 d\Omega}{4\pi A} N S(\mathbf{k}, \omega) d\omega (1 - \cos^2\theta), \tag{2.20}$$

Where $d\Omega$ is the solid angle, $d\omega$ is the frequency interval, P_0 is the power of the x-ray probe, r_0 is the classical electron radius, A is the cross sectional area encountered by the x-ray probe, N is the total number of electrons, and $S(\mathbf{k}, \omega)$ is the dynamic structure factor (DSF).

The DSF is the space-time Fourier transform of the density-density correlation function [73, 35]. This term accounts for the density fluctuations and is dependent on the plasma conditions. The Chihara formalism [18, 19] is commonly used to evaluate the DSF. This formalism separates the total electron population into two groups, the electrons bound to ions and the free electrons. This formalism is strictly applicable to plasmas with one ion species, but there is ongoing research to generalize to multi-species plasmas [100]. The DSF with the Chihara formalism is given as

$$S(k, \omega) = |f_I(k) + q(k)|^2 S_{ii}(k, \omega) + Z_f S^0_{ee}(k, \omega) + Z_b \int d\omega' \tilde{S}_{ce}(k, \omega - \omega') S_S(k, \omega'). \tag{2.21}$$

The first term in the Chihara DSF is the elastic scattering feature, which accounts for scattering from electrons that follow the motion of the ions. Screening from the valence electrons is given by $q(k)$, $f_I(k)$ is the ion form factor which accounts for bound electrons, and $S_{ii}(k, \omega)$ is the ion-ion structure factor. The remaining two

terms describe the inelastic scattering feature. The second term describes free-free scattering, where Z_f is the number of free electrons and S_{ee}^0 is the electron-electron structure factor. The final term accounts for bound-free scattering, where Z_B is the number of bound electrons, $\tilde{S}_{ce}$ is the structure factor of the core electrons. S_S is the self ion structure factor. The experimentally obtained x-ray scattering spectrum is compared to theoretical spectra generated by varying the plasma conditions in the DSF to determine temperature and ionization that provides the best fit.

2.2.4.1 Imaging X-ray Thomson Spectrometer

The imaging x-ray Thomson spectrometer (IXTS) [30] was the main diagnostic for this dissertation work due to the ability to spectrally resolve scattered x-rays while imaging in 1-D. The imaging component allows XRTS measurements in systems where there might be 1-D gradients, such as in a planar laser-driven shock wave experiment. The IXTS was developed under collaboration between the University of Michigan and Los Alamos National Laboratory prior to this work.

The crystal in the IXTS is a toroidally bent Ge(220) crystal, with radius of curvatures of 10 and 100 cm, and a Bragg angle of 23.4° for 7.8 keV photons. The distance from source to crystal is 19.1 cm and the distance from crystal to detector is 39.6 cm, giving a magnification of 2.07. The IXTS can use a CCD or an image plate as a detector and has a spectral resolution of about 5 eV and spatial resolution of about 50 microns [29].

CHAPTER III

Platform Development for Studying Shocked Foams on OMEGA EP

3.1 Introduction

This chapter presents experimental work on developing a platform to study laser-driven shock waves in foam using the imaging x-ray Thomson spectrometer (IXTS) on the OMEGA EP laser facility. The IXTS was previously used on OMEGA 60 laser facility to obtain a density profile, and infer temperature and ionization of shocked carbon foams [28]. These experiments were limited to driving the shock wave for 1 ns, corresponding to the pulse length of the laser. This motivated studying shocked foams on the OMEGA EP laser system where the shock wave can be driven up to 10 ns, producing post-shock plasma conditions having smaller gradients.

The OMEGA EP laser system provides an experimental geometry challenge with using the IXTS, however. One of the OMEGA EP beams is used to drive the shock, while the remaining three beams are used to generate the x-ray probe. The IXTS, which measures the scattering of the x-ray probe, is only qualified for one diagnostic port, TIM 14, in the OMEGA EP laser chamber. The combination of all four OMEGA EP beams coming in from roughly the same direction, and the fixed location of the diagnostic, severely limited and complicated the experimental geometry. This chapter

is based upon of a paper written by the author, entitled "Demonstration of imaging X-ray Thomson scattering on OMEGA EP", which appeared in *Review of Scientific Instruments* in September 2016.

3.2 Experimental Setup

A schematic of the experimental geometry is given in Figure 3.1 A).The main foam package was irradiated with a 10 ns, 4 kJ laser beam equipped with a phase plate (WEP-750-SG8) providing a 750 μm diameter laser spot size and eighth-order super-Gaussian intensity distribution, yielding a laser intensity on target of 7×10^{14} W/cm^2. The foam package consists of three layers. The laser irradiates the first layer, which consists of a 50 μm plastic (CH) ablator. The middle layer was 28 μm of quartz, included to protect the foam from heating due to the laser interactions driving the shock wave. The final layer was 1.5 mm of resorcinol formaldehyde (RF) foam, with a measured composition of 39.4% hydrogen, 16.2% oxygen, 44.3% carbon, and trace amounts of nitrogen, and with a density of 340 mg/cm^3. The manufacturing of the foam package was carefully designed to prevent gaps between the layers. The plastic ablator layer was glued on one side of the quartz, while the foam was grown on the opposite side without any glue.

At a specified time delay, the remaining three OMEGA EP beams, with a pulse length of 2 ns, 6 kJ of total energy, WEP-750-SG8 phase plates, and overlapped laser intensity of $\sim 1 \times 10^{14}$ W/cm^2 irradiated a nickel foil to generate the 7.8 keV nickel He-α like lines. A 1 mm thick copper collimator with an 800 μm opening diameter was located between the foam and the x-ray source and restricted the incident angle of the x-rays. A 1 mm x 0.5 mm window in the gold shielding between the foam and the detector limits the observed foam volume and provides a scattering angle of $90\pm20^\circ$.

The components were placed in 3-D printed scaffolding for ease of assembly, shown

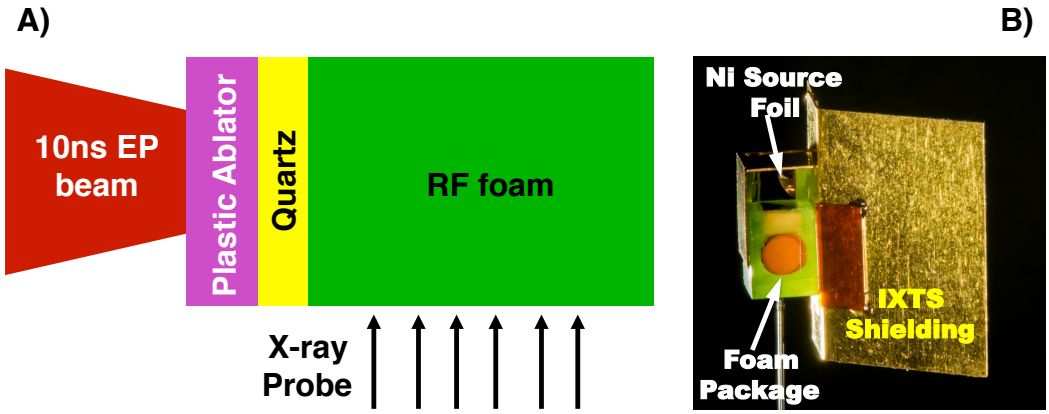

Figure 3.1: A) Schematic of experimental geometry and foam package. A long pulse laser, depicted in red, irradiates the foam package. The foam package consists of an ablator layer in purple, a quartz heat shield in yellow and the 340 mg/cc resorcinol formaldehyde foam in green. The x-ray probe enters the shocked foam from the bottom, and the IXTS, located out of the page, collects the scattering of the probe. (B) Photograph of assembled target. The green 3-D printed scaffolding houses the important target components. The orange foam slides into a slot within the scaffolding, and the nickel foil used to generate the x-ray probe is glued onto the scaffolding. Large gold foils that are used as shielding for the IXTS are also glued to the scaffolding. The window to the IXTS is on the opposite side of the target.

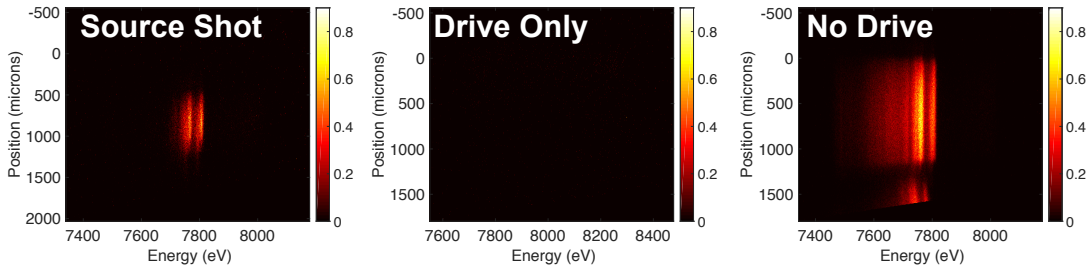

Figure 3.2: The first three shots obtained ancillary data for the experiment. The first shot measured the generated x-ray source spectrum, which is needed to analyze the scattered spectrum in later shots. The Drive Only shot was included to isolate any background sources produced by the laser driving the shock wave. No appreciable background was detected. The No Drive shot was used to determine background from generating the x-ray probe. This shot measured background comparable in signal to the scattered measurement, however the background was spatially separated from the data.

in Figure 3.1 B). Due to the four laser beams arriving on the target from almost the same direction within a 45° full angle, the laser-irradiated side of the nickel foil faces the foam package. Large gold foils were attached to the scaffolding and used as shielding to protect the IXTS measurement from background x-ray sources. The primary sources of background were the hot blow-off plasmas from driving the shock wave and producing the x-ray source. The window in the gold shielding to the IXTS is located on the other side of the shield and is not visible in Figure 3.1 B). The primary challenge in developing this experimental platform was finding the combination of backlighter target geometry and shielding that would produce good quality data.

3.3 Experimental Results

The experiment successfully obtained data for eight laser shots. The first three shots are given in Figure 3.2. The first shot measured just the spectrum of the x-ray source, which is important for analyzing the scattered spectrum on subsequent shots. The second shot was a drive only shot to check for sources of background produced by the drive laser beam. From this shot, we concluded that there was no appreciable

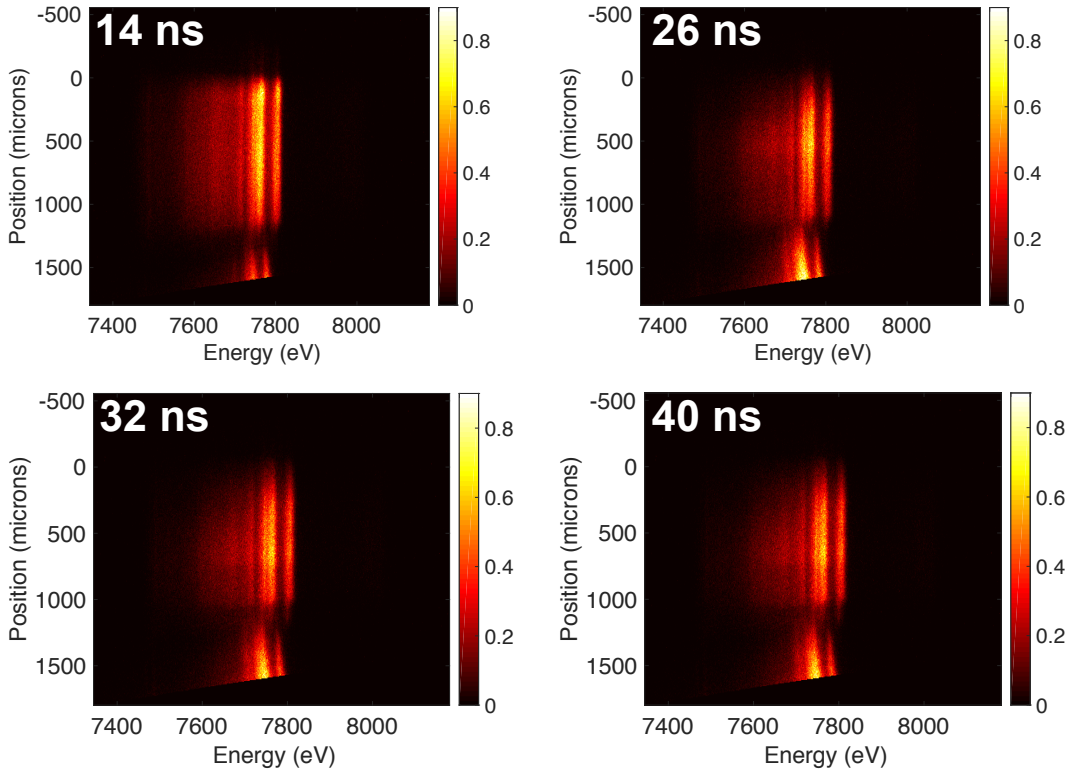

Figure 3.3: IXTS data images at four different time delays between the drive beam and the probe beams. Note that each time delay corresponds to a separate shot. In general, regions of high x-ray intensity correspond to regions of higher mass density, and can be useful to qualitatively track the shock with different probe times.

background due to the laser drive. The third shot consisted of the three beams used to generate the x-ray probe. This shot included background, however it was spatially separated from the measurement, so minimal data was compromised. This shot can also be used as a measurement of an unshocked foam.

The remaining five shots consisted of measuring the shock at different times by changing the delay between the three probe beams and the drive beam. Figure 3.3 shows the data for probe times of 14, 26, 32 and 40 ns. Figure 3.4 gives the data at 20 ns, which includes a schematic to the orientation of the measurement. The data at 20 ns will be used as an example later in the chapter to show the analysis approach.

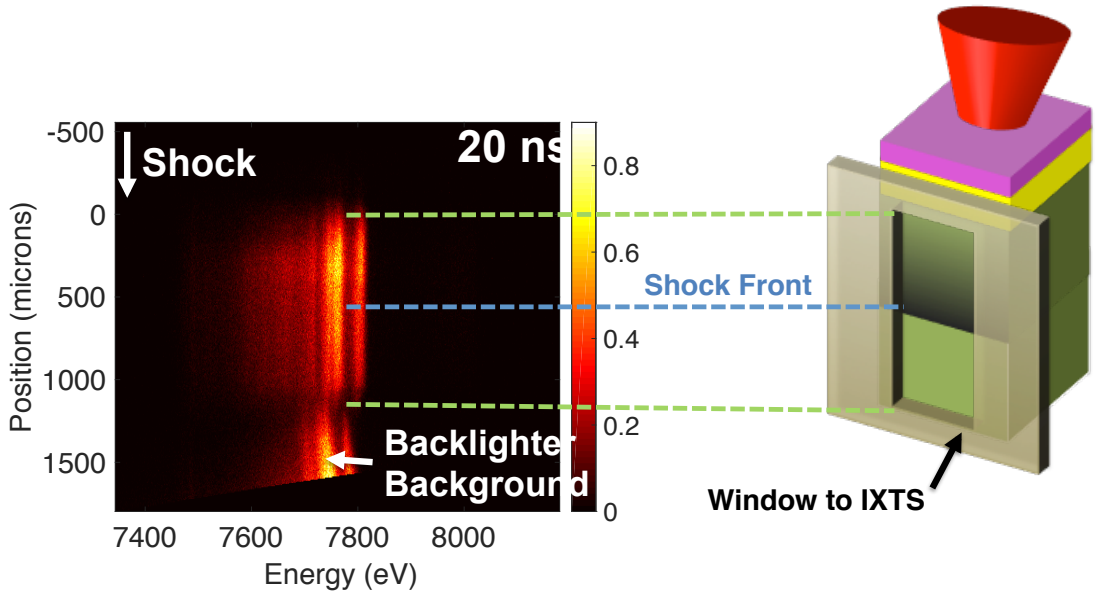

Figure 3.4: Intensity of scattered x-rays taken with the IXTS at 20 ns after the start of the drive laser. A 3-D cartoon is also included to give orientation of the measurement. The colors are the same as Figure 3.1, where the red cone represents the laser beam, the purple layer is the plastic ablator, the yellow layer is the quartz heat shield, and the green is the RF foam. The background from the x-ray source is identified, and the direction that the shock is traveling is given for reference. The shock front is obtained from ray tracing analysis discussed later in the chapter, and is included here for reference.

3.3.1 Ray Tracing Analysis of the Spatial Profile

Qualitatively, Figures 3.3 and 3.4 shows that the most intense regions of scattered x-ray signal are changing with time. To analyze the density profile further, lineouts were taken along the 7.8 keV elastic scattering peak. Figure 3.5 gives the lineout at 7.8 keV at 20 ns plotted in black. The elastic scattering is predominantly from the two electrons in the 1s shell of the carbon atom. Since we are expecting ionizations under 4, the strength of the elastic scattering is proportional to the number of carbon atoms in a volume, or the mass density.

The measured profile is not directly proportional to density however, due to attenuation of the x-ray probe as it is traversing through shocked foam to the scattering volume, and then the scattered probe attenuating as it traverses to the detector. The measured elastic scattering signal can be expressed as

$$I_{el} \propto I_0 \left[e^{-\tau_1}\right] [\rho] \left[e^{-\tau_2}\right], \tag{3.1}$$

where the first term represents attenuation of the x-ray probe to the scattering volume, the second term accounts for elastic scattering of the beam and is proportional to the mass density, and the third term accounts for the attenuation the scattered probe as it goes to the detector. Here $\tau = \int_{x_0}^{x_1} \rho(l)\mu(l)dl$ is the optical depth, I_0 is the initial intensity of the probe, ρ is the density, and μ is the mass attenuation coefficient. In a lot of practical applications, the optical depth can be challenging to solve analytically due to complicated geometries.

To solve Equation 3.1, we use the method of ray tracing analysis, which discretizes the density and mass attenuation coefficient onto a grid so that the solution can be found numerically. The discretized version of Equation 3.1 can be expressed as

$$I_{el} \propto I_0 \rho_e \left[\prod_{i=0}^{n} e^{-\rho_i \mu_i \Delta x_i}\right] \left[\prod_{j=n}^{m} e^{-\rho_j \mu_j \Delta x_j}\right]. \tag{3.2}$$

Here ρ_e is the density of the cell where elastic scattering occurs, Δx is the path length of the x-rays through the cell, the first bracket is the attenuation of the probe to the cell where elastic scattering occurs, and the term in the second bracket is the attenuation of the scattered ray to the detector. Stepping through each cell that the ray travels through solves equation 3.2.

The density matrix that is needed to solve Equation 3.2 is found by running the 1-D hydrodynamics code *HYADES*. The *HYADES* simulations were run with an ideal gas equation of state with an adiabatic index γ that varied from 1.6 to 2, and a scaling of the laser intensity ranging from 50% to 100%. The variable adiabatic index and laser intensity scaling gave parameters that could be tuned to fit the data. The calculated density profiles were then projected into 3-D to create a planar shock wave. X-rays from a source with a realistic spatial distribution were sent along the collimator axis into the foam and scattered by 90° through the Au shield to the diagnostic. The source spatial distribution was assumed Gaussian and fitted to match the measured scattering profile from an unshocked sample. Motion blurring and detector resolution were also taken into account with this analysis.

Figure 3.5 shows the result of the analysis. The black line is the measured spatial profile, the red line is the *HYADES* profile used for ray tracing, and the blue line is the result from the ray tracing analysis. The ray tracing analysis showed that that the inflection point in the measured profile close to its peak approximately gives the shock front location. The compression is estimated to be 3 ± 1 at 20 ns.

The ray tracing analysis was repeated for each probe time obtained during the experiment. Perfect matches were not obtained for each time, likely caused by the Hyades simulation being run in 1-D. The shock front location could still be determined from the inflection in the data. The estimated shock front location is plotted in Figure 3.6, with the error bars representing the uncertainty of identifying the inflection point. The shock speed in the foam was found by fitting a line to the shock front location in

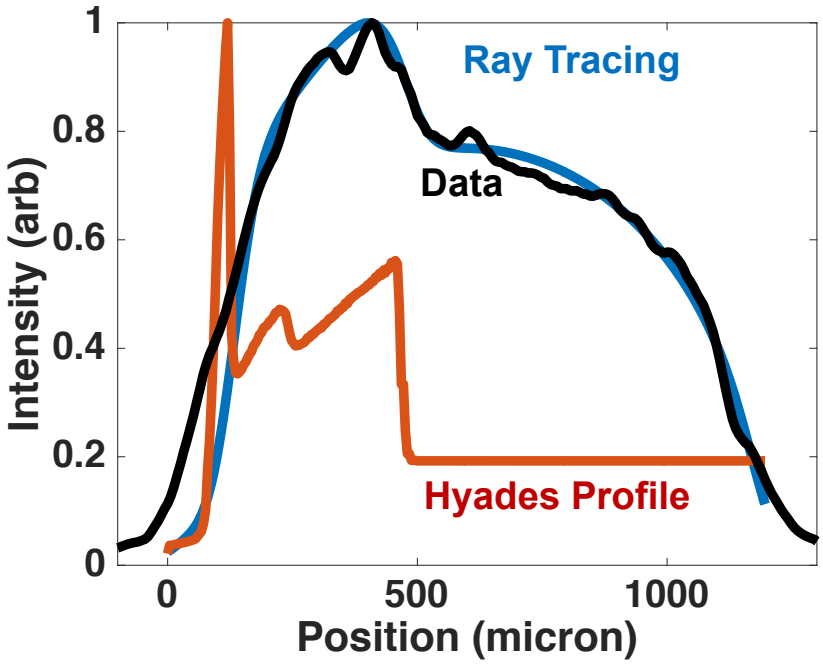

Figure 3.5: Comparison of 1-D *HYADES* mass density profile in red with data profile taken at 20 ns in black and the resulting ray trace analysis in blue.

Figure 3.6. The shock speed is estimated to be 39±6 km/s until 26 ns, and then the speed falls off at later times. The error in shock speed is estimated by incorporating the uncertainty in the shock front location. This result is in reasonable agreement with the *HYADES* simulation with $\gamma = 2$ and I =75% I_0, where the shock speed is 45 km/s. Similar simulations with the 1-D radiation hydrodynamics code *LILAC* [23] were performed by collaborators at the Laboratory for Laser Energetics, with a 10 ns pulse, an intensity of 1.2×10^{14} W/cm^2, and 23° angle of incidence. A simulation with 50% reduced intensity produced a shock velocity of 45 km/s, which is reasonably consistent with the *HYADES* simulation.

3.3.2 XRTS Analysis

With the density profile analyzed, the spectrum at different regions in the foam can be inspected. Figure 3.7 shows the spectral data for probe delay of 20 ns at upstream of the shock front, down stream of the shock front, and at the shock front

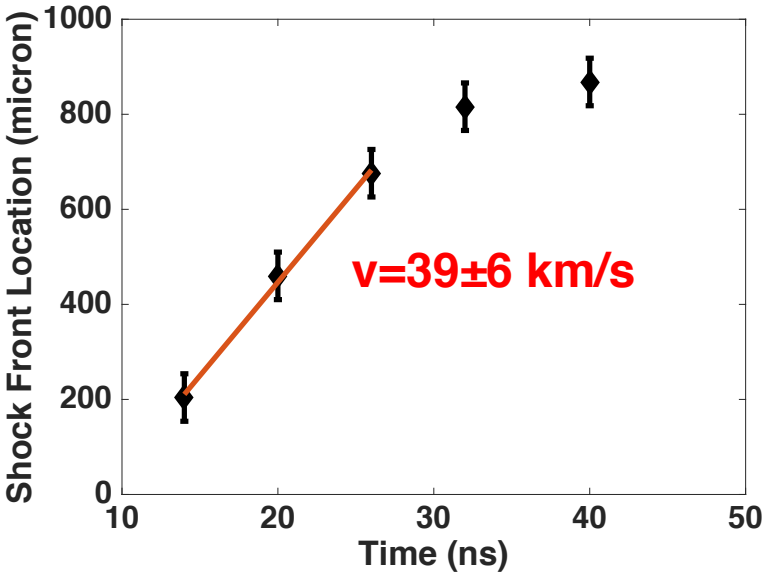

Figure 3.6: The inflection point in the data identifies the location of the shock front for each time delay. The error bars correspond to approximate uncertainty in identifying the inflection. The average shock speed is found by fitting a line to the first three time points.

as identified by the inflection point. Note that there is no appreciable difference in the scattering spectra for different regions of the shock profile. This is a result of x-ray Thomson scattering being insensitive to ionization for weakly ionized carbon and oxygen for this x-ray energy [81].

Theoretical spectra were calculated with the xrs.x code [35]. The compression was assumed to be 3 from the ray tracing analysis, and the hydrogen was assumed to be full ionized, $Z_H = 1$, and the ionization for carbon and oxygen was assumed to be 2, $Z_O = Z_C = 2$. The theoretical spectra are compared to the measured spectrum at the shock front in Figure 3.8, resulting in an inference of a shock temperature of less than 20 eV.

3.3.3 Photonics

The photonics calculation estimates the number of measured scattered photons in an XRTS experiment[34]. For practical purposes, the absolute result of the calculation

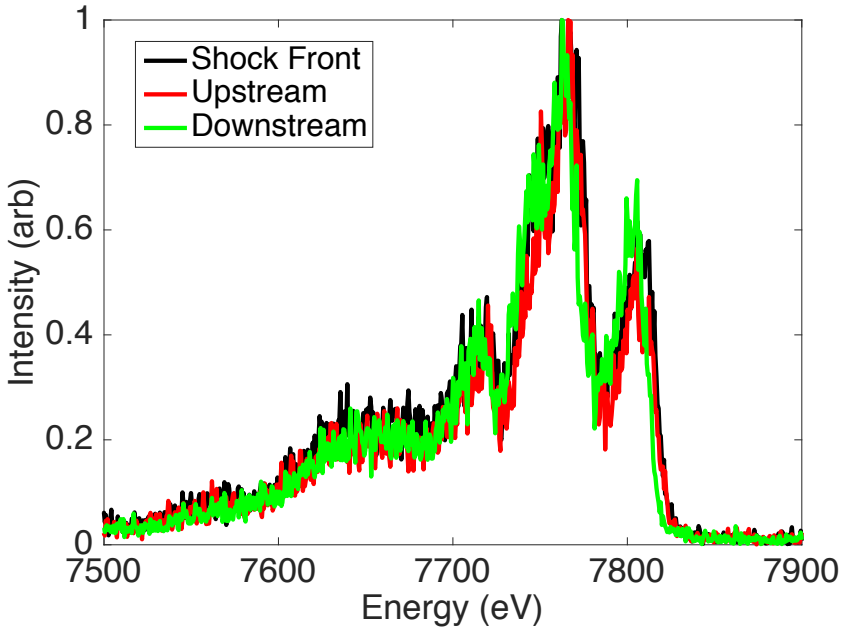

Figure 3.7: X-ray scatter spectra at probe time of 20 ns given for upstream of the shock front in red, downstream of the shock front in green and at the shock front in black.

is not necessarily reliable because several of the parameters are vague estimates with large uncertainties, and the fact the detector is usually not absolutely calibrated. The power of the photonics calculation is that it gives a clear way to predict impact from changing experimental conditions from one experiment to another. The calculation of the number of photons is given below, along with comments on where improvements could be made.

The number of measured scattered photons is

$$N_D = \left[\frac{E_L}{h\nu}\eta_x\right]\left[\frac{\Omega_{pl}}{4\pi}\eta_{att}\right]\left[\frac{n_e\sigma_{th}l}{(1+a)^2}\right]\left[\frac{\Omega_{det}}{4\pi}\eta_s DQE\right]. \tag{3.3}$$

The first bracket represents the conversion of laser photons into x-ray probe photons. Here E_L=6kJ is the laser energy used to produce the x-ray probe, $h\nu$=7.8 keV is the photon energy of the x-ray probe, and η_x=0.005 is the efficiency for converting laser energy into 7.8 keV x-rays. In this experiment the x-ray probe energy is fixed

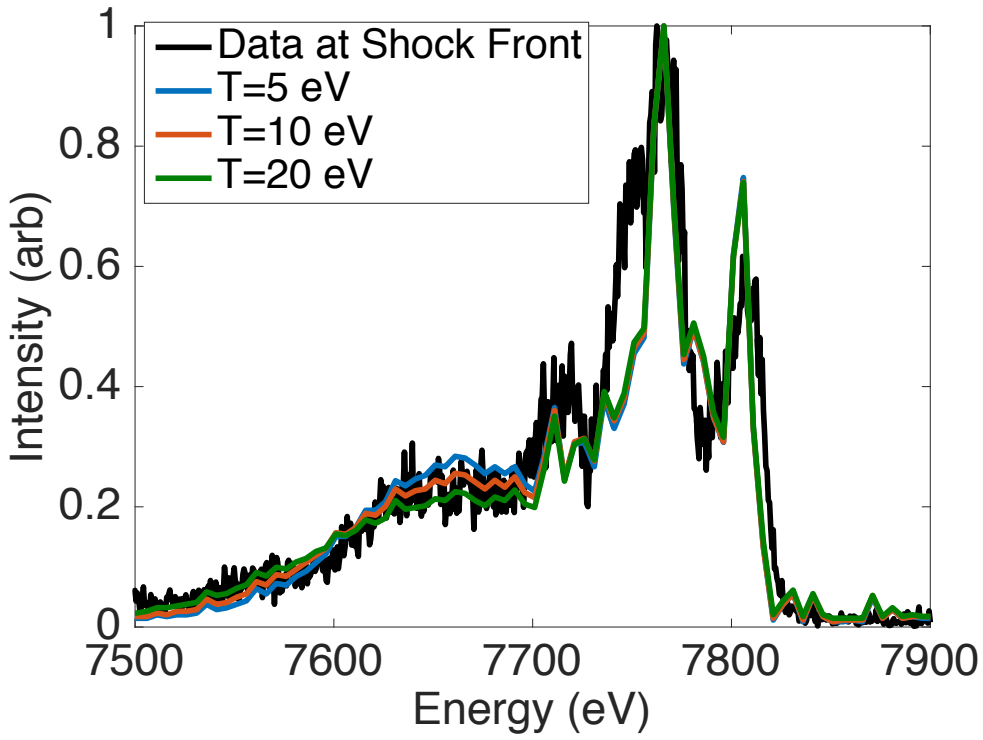

Figure 3.8: Experimental scattered x-ray spectra taken at 20 ns at the shock front location compared to theoretical spectra of different temperatures.Theoretical spectra calculated with compression=3, $Z_{\mathrm{C}} = 2$, $Z_{\mathrm{O}} = 2$ and $Z_{\mathrm{H}} = 1$.

by the diagnostic, and the laser is being operated at max energy. Increasing the laser intensity to $\approx 1\times10^{15}$ W/cm^2 through decreasing the spot size could increase the conversion efficiency, as mentioned in Chapter 2.

The second bracket accounts for the number of photons that actually make it to the scattering region. Here Ω_{pl} is the solid angle of the scattering volume with respect to the source, and is estimated to be 0.5 sr by $\Omega_{pl} = \frac{\pi r_{col}^2}{length_{col}^2}$, where $length_{col}$ is the length of the collimator and r_{col} is the radius of the collimator. $\eta_{att} = e^{-\rho\mu L}$ is the transmission of the x-rays through the RF foam, where ρ is the shocked mass density, μ is approximated as the mass attenuation coefficient for materials at room temperature, and L is the length to the scattering volume. The transmission was found to be 0.79. Optimizing the copper collimator could change the solid angle, and changing the density or the foam material will impact the transmission.

This third bracket calculates the number of photons that are scattered in the plasma. Here n_e =7e22 cm^{-3} is the electron density, σ_{th}=0.66e-24 barns is the usual Thomson scattering cross section, and l =1mm is the scattering length. Since this experiment is in the noncollective geometry, $(1 + a)^2 = 1$. The most straightforward parameter to change is the electron density by increasing the mass density of the foam, however this will also decrease the transmission in the second bracket.

The fourth bracket accounts for the number of photons that are actually measured by the detector. Here Ω_{det} is the solid angle to the detector, DQE is the quantum efficiency of the detector, and η_x is the transmission through any detector shielding. All of the terms here are constrained by the diagnostic geometry, and no offer straightforward path for changes.

To summarize, the changes to the experimental design that could increase the number of scattered photons measured include optimizing the generation of the x-ray probe, changing the collimator geometry, and changing the foam density and material. Note that a lot of the parameters are interdependent with each other, so care must

be taken to optimize the entire process.

3.4 Conclusion

Imaging x-ray Thomson scattering has been successfully demonstrated for the first time on OMEGA EP. From the spatial data we clearly observe a shock wave at different probe times as it traverses the foam. We were not able to obtain appreciable difference in scattering spectra at different locations along the shock profile due to weak shock heating and poor signal. Changes to the design to increase the measured signal was explored.

CHAPTER IV

Spatially Resolved X-ray Thomson Scattering Measurements of Shocked Carbon Foams

4.1 Introduction

This chapter discusses the experimental design and results of shocked carbon foam on OMEGA EP. The experimental design was based off of the design presented in Chapter 3 with changes to optimize performance of the x-ray source and shock wave. The imaging x-ray Thomson spectrometer is used to obtain inferences of compression, shock temperature, and shock velocity of the shocked carbon foam. These inferences were compared to Hugoniot calculations of LANL SESAME equation of state tables for carbon.

4.2 Experimental Setup

The experimental target design was based upon the target described in Chapter 3, with modifications to the x-ray source and foam to obtain higher quality data. The basic geometry of the experiment is the same as Chapter 3, except for the x-ray source, which will be detailed below. This section is divided into two subsections, foam package and x-ray source, which roughly separates the sections of the target based on the two areas that are being irradiated with laser beams.The target design

is discussed and a discussion of the changes made to the target is included in each subsection. The target detailed in Chapter 3 will be referred to as the initial target design.

4.2.1 Foam Package

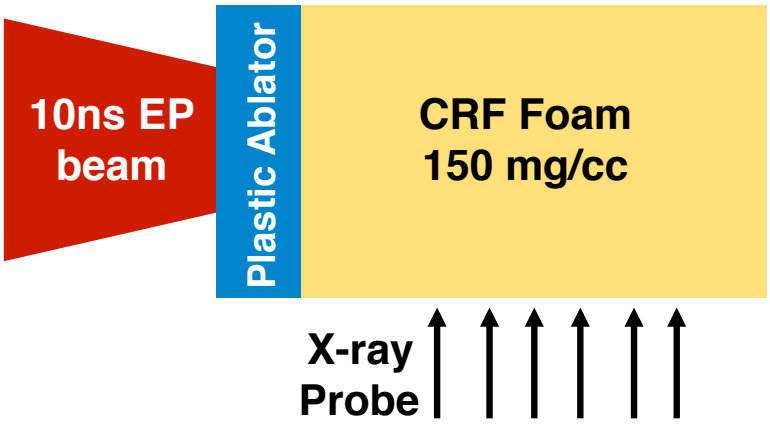

Figure 4.1: Schematic of experimental geometry and foam package. A long pulse laser, depicted in red, irradiates the foam package. The foam package consists of an ablator layer in blue, and the 150 mg/cc carbon foam in yellow. The x-ray probe enters the shocked foam from the bottom, and the IXTS, located out of the page, collects the scattering of the probe.

One OMEGA EP beam was used to drive a shock into a foam package. The beam contained 4.3 kJ of energy in a 10 ns square pulse with wavelength of 351 nm. The beam was equipped with a distributed phase plate (SG8-750) providing a spot size of 750 μm, producing an intensity of 1×10^{14} W/cm^2. The foam package consisted of a 50-μm-thick plastic (CH) ablator layer, and a 2-mm-long carbonized resorcinol formaldehyde (CRF) foam with an initial density of 150 mg/cm^3. The layers were press fitted into a 3-D printed super structure to avoid having a glue layer. Figure 4.1 shows a cartoon of the target geometry.

Changes from the initial target design

The foam package contained numerous changes from the initial target design. The first change involved the removal of the quartz heat shield. The quartz heat shield was initially included to filter high energy x-rays that are produced during laser ablation to drive the shock wave into the foam, however the experiment in Chapter 3 observed no evidence of a significant amount of high energy x-rays from the driving of the shock wave. The quartz layer then added an additional obstacle to the shock wave before reaching the foam, adding additional complications and uncertainty in predicting the timing of the shock for measurements.

The second change to the foam package consisted of changing the foam properties. The foam material was changed from resorcinol formaldehyde (RF) to CRF. The RF foam contained at least three elemental species, carbon, oxygen, and hydrogen, in similar proportions, which made the x-ray Thomson scattering analysis extremely difficult. The change to CRF foam, which is predominantly carbon, simplified the analysis. The foam density was also decreased from 340 mg/cc to 150 mg/cc. The lower density allowed for a stronger shock to be driven into the foam and less attenuation of the x-ray probe beam.

The final change was the assembly of the foam package. The initial target design involved growing RF foam onto the rear surface of the quartz heat shield and gluing the plastic ablator to the front surface. The process of producing CRF foam involved heating RF foam to high temperatures to remove the hydrogen and oxygen, which prevented growing the foam onto the plastic ablator. The plastic ablator and CRF were press fitted together, to avoid a glue layer that may wick into the foam structure.

4.2.2 X-ray Source

At a specified delay time after the start of the drive beam, the remaining three OMEGA EP beams illuminated a Ni foil to generate a burst of He_α line emission at

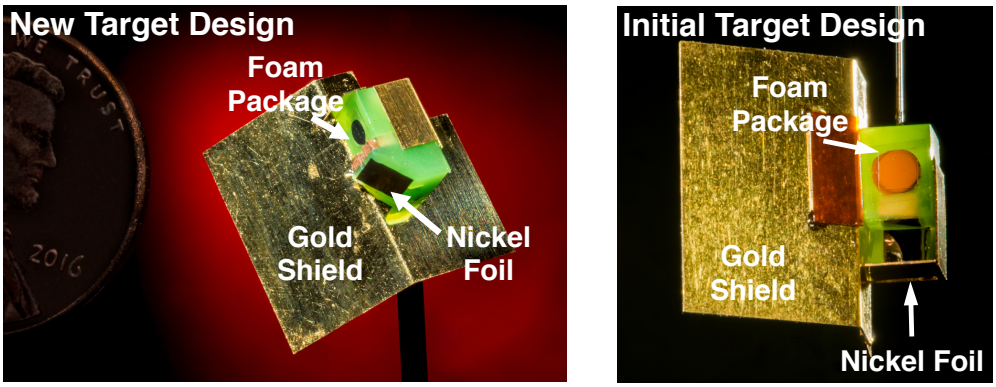

Figure 4.2: The photograph on the left is a target similar to the target used in the experiments detailed in this chapter. The photograph on the right is the target from Chapter 3. Noticeable visual differences include the change to the nickel foil geometry and the change to CRF foam (black) from RF foam (orange).

7.8 keV. The beams had a total energy of 3.75 kJ in a 1 ns square pulse at 351 nm wavelength. One of the probe beams used SG10-400 distributed phase plate, while the remaining two beams were focused to a 400 μm laser spot on target. Two copper blocks with 500 μm separation were located between the foam and Ni foil to collimate the x-rays. The scattering angle is 65 $\pm 10°$. The foam package, copper collimator and nickel foil were assembled into a CH super structure to ensure consistent alignment. Gold foil shielding attached to the super structure protected the IXTS diagnostic from background. A 1.2 mm by 0.5 mm window was cut into the shielding and the super structure to collect the scattered x-rays from the shocked foam.

Changes from the initial target design

The x-ray source and collimator was completely redesigned for this experiment. The collimator was changed from a circular aperture to a rectangular aperture. The aperture serves to restrict the volume of shocked foam probed, as well as to restrict the incident angles of the x-rays to constrain the scattering angle. In the probe geometry feasible due to geometry constraints by the facility, the ideal x-ray probe would be a 1-D sheet of x-rays that uniformly probe the shock profile. The cartoon version of this

probe is given in Figure 4.1. The circular aperture imposed unnecessary geometric modifications to the imaging portion of the measurement.

The x-ray source was also completely redesigned, as shown in Figure 4.2. The nickel foil geometry was restructured so that the shocked foam observed emission from the rear side of the foil, which served as a filter for a small portion of the background experienced in the initial spectra. Further changes included reducing the pulse length of probe beams from 2 ns to 1 ns. Motion blurring was a concern due to the expected increase in shock velocity from lowering the foam density. Due to facility laser power restrictions, the energy of the laser beams had to be reduced from 6 kJ to 3.75 kJ. To compensate for the reduced laser energy, the spot size was reduced from 750 μm to 400 μm. These changes increased the laser intensity by an order of magnitude, and into the regime of highest conversion efficiency, as discussed in Chapter 2.

4.3 Experimental Results

The shot day successfully obtained eight measurements with the IXTS diagnostic. The first three shots are given in Figure 4.3, and include a source shot, a drive only shot and a no drive shot. The source shot is important for analyzing the spectral data, and was obtained by pointing the IXTS to look directly at the nickel foil. The drive only shot did not use the lasers for generating the x-ray source, and confirmed that there was no appreciable background from driving the shock wave. Only the three lasers used to generate the x-ray source was operated in the no drive shot. Diffuse background is present in the lower half of the data. Future shots were restricted to the top half region of the data, which resulted in a maximum probe time of 16 ns.

The remaining IXTS data is given in Figures 4.4 and 4.5. The IXTS collected data at probe times of 12.5, 13, 14, 15, and 16 ns. The data at 15 ns, which is given in Figure 4.5, will be used to show an example of the analysis in the section below.

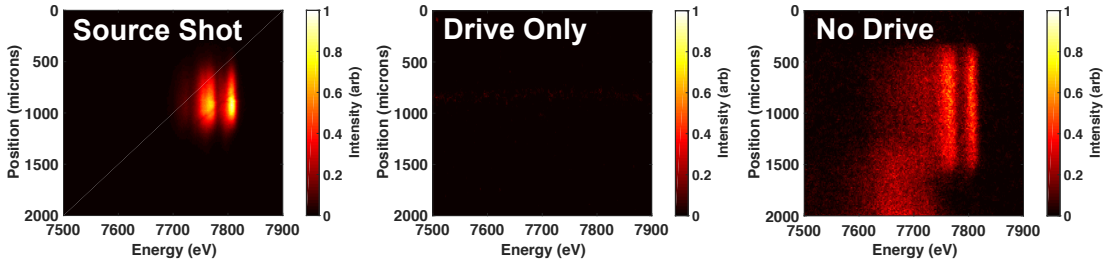

Figure 4.3: The first three shots obtained ancillary data for the experiment. The first shot measured the generated x-ray source spectrum, which is needed to analyze the scattered spectrum in later shots. The Drive Only shot was included to isolate any background sources produced by the laser driving the shock wave. No appreciable background was detected. The No Drive shot was used to determine background from generating the x-ray probe. This shot measured background comparable in signal to the scattered measurement, located on the lower half of the measurement.

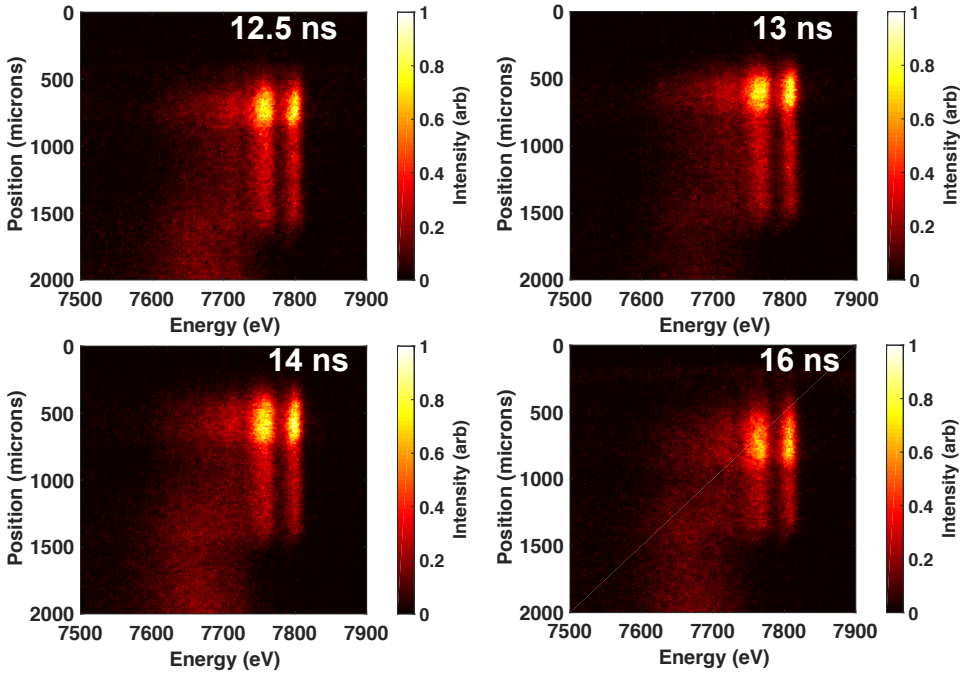

Figure 4.4: IXTS data images at four different time delays between the drive beam and the probe beams. Note that each time delay corresponds to a separate shot.

4.3.1 Ray Tracing Analysis

The strength of the measured elastic scattering signal gives information about the density of the shocked foam. The x-ray probe beam is attenuated while traversing

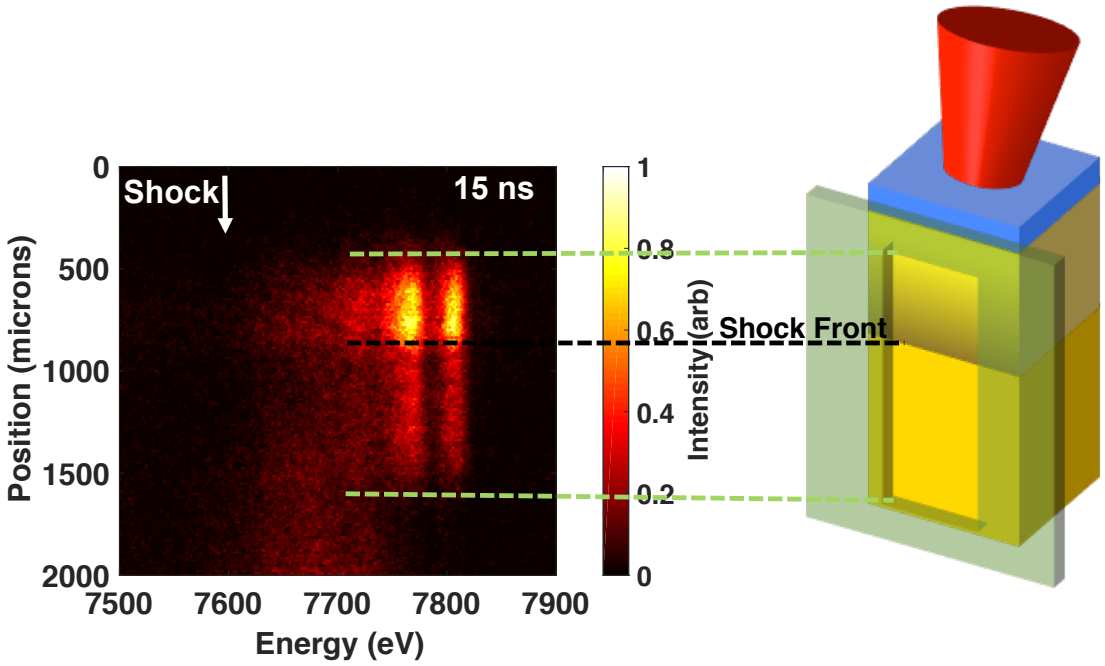

Figure 4.5: Intensity of scattered x-rays taken with the IXTS at 15 ns after the start of the drive laser. A 3-D cartoon is also included to give orientation of the measurement. The colors are the same as Figure 4.1, where the red cone represents the laser beam, the blue layer is the plastic ablator, and theyellow is the carbon foam.

through the different density regions in the shocked foam. The strength of the scattered signal depends on the strength of the probe beam at the scattering volume, and on the subsequent attenuation of the scattered signal. Compression and shock location inferences is obtained with ray tracing analysis, which is covered in Chapter 3 but a synopsis of the method is given below.

We began with a 1-D radiation-hydrodynamic simulation (HYADES) with an ideal gas equation of state. By varying the laser intensity and the adiabatic index, γ, different density profiles with different shock speeds are generated. The HYADES simulations are projected into 3-D to create a planar-shock-wave profile. X-rays with the measured 1-D spatial intensity distribution are injected along the centerline of the shock wave. The attenuation of the probe beam is tracked and elastic scattering is calculated when the x-rays enter the scattering volume as defined by the window

to the IXTS. The attenuation of the scattered x-ray probe is tracked and the x-ray count is recorded. This method also takes into account the detector resolution and motion blurring. This method is ideal due to being relatively simple and not too computationally expensive.

The result from the analysis is given in Fig. 4.6 A). A goodness of fit metric,

$$\chi^2 = \sum_i \frac{(R_i - M_i)^2}{M_i}, \tag{4.1}$$

where R_i is the result of the ray tracing, and M_i is is the measured quantity, was used to determine the best fit. The absolute values are not known since the detector was not absolutely calibrated, so the uncertainty was estimated by the doubling of the χ^2 value. We infer a compression of 4±1 at 15 ns from this analysis, and the results of the other shots are plotted in Figure 4.9 A).

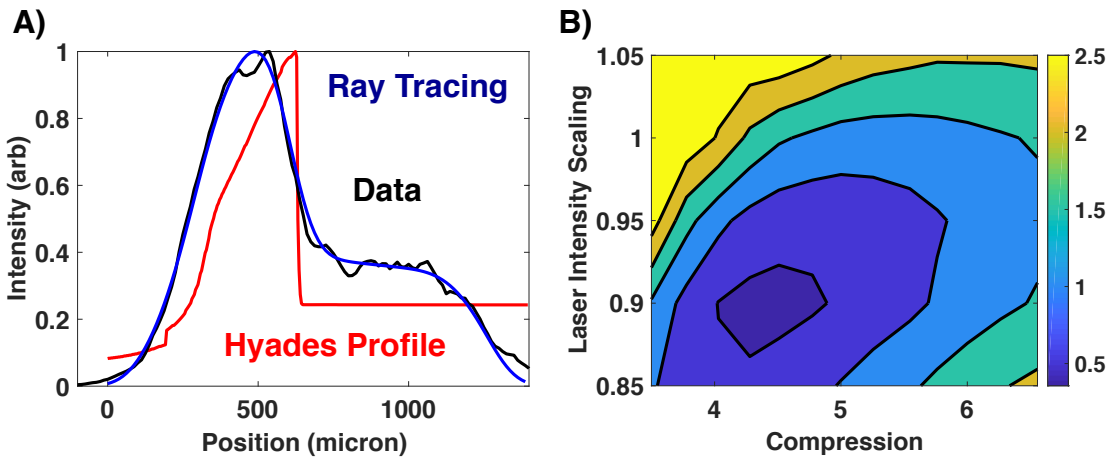

Figure 4.6: A) Spatial profile of ray tracing analysis (blue), with the simulated 1-D HYADES density profile (red) compared to the experimentally measured profile (black). B) χ^2 fit between the measured spatial profile and ray tracing using variable adiabatic index and laser intensity scaling.

A shock velocity was inferred by tracking the shock front over multiple shots with the different probe times, as shown in Figure 4.7. We estimate an average shock velocity of 78 ± 37 km/s by fitting a line to the shock front locations. Note that

the data point at 12.5 ns appears to be an outlier, and removing the 12.5 ns data point from the shock velocity fit yields an average shock velocity of 98 $\pm$ 25 km/s. A deviation from the target design could explain the outlier point. For example, if the target that was used for the 12.5 ns shot had a thinner ablator, then the transit time of the shock in the ablator would be reduced. Similarly, a misalignment of the window to the IXTS and a lower foam density could also contribute to the uncertainty in the target. Ultimately we could not specify and correct for any aberration in the target assembly for the 12.5 ns target, and therefore we were unable to determine a suitable reason to exclude this data point from the analysis.

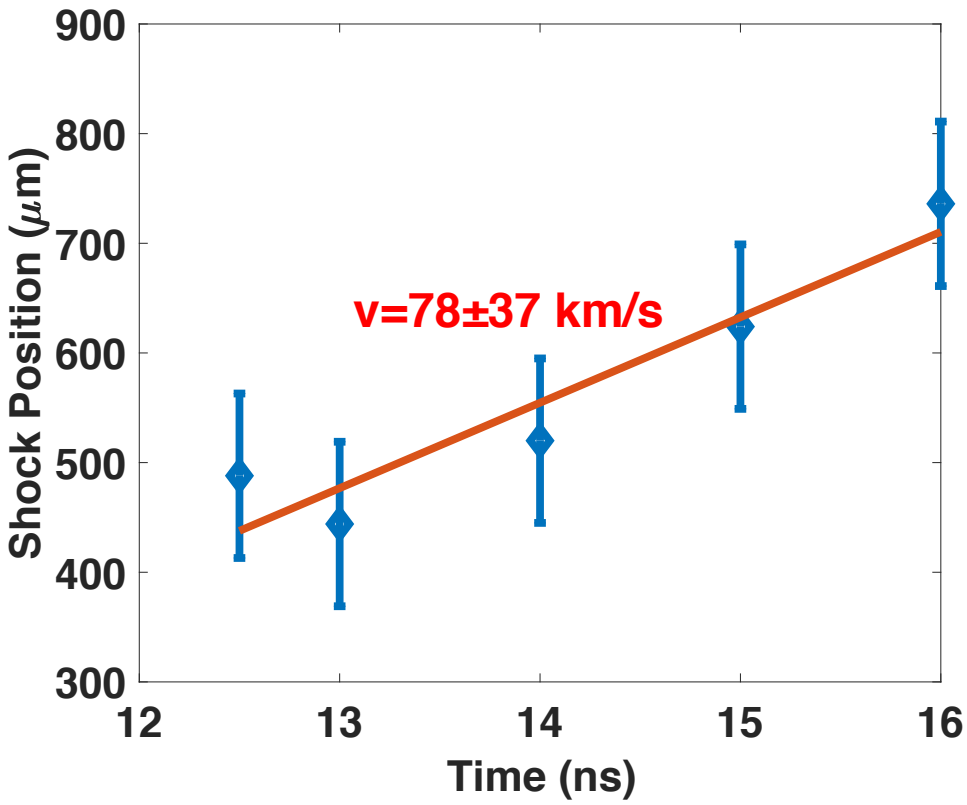

Figure 4.7: Shock front determined from ray tracing analysis for each time delay. The error bars correspond to approximate uncertainty in the ray tracing analysis. The average shock speed is found by fitting a line to the points.

4.3.2 XRTS Analysis

Temperature and ionization can be inferred by analyzing the scattered x-ray spectra. The theory of x-ray Thomson scattering (XRTS) is given in Chapter 2, and a recap is given below.

The scattering parameter α, where $\alpha = \frac{1}{k\lambda_s}$, is useful for determining the scattering regime[80] measured by the IXTS. Here $k = \frac{4\pi}{\lambda_0} \sin \frac{\theta}{2}$ is the scattering vector, given as a function of scattering angle θ and probe wavelength λ_0, and λ_s is the shielding length. For parameters of this experiment, $\alpha = 0.1$ which means we measure scattering from the individual electrons, or non-collective scattering.

A lineout at the shock front yields the scattered x-ray spectrum, and is plotted in black in Figure 4.8 A). The xrs.x program[35] was used to calculate the dynamic structure factor for various plasma conditions to compare with the measured spectrum. The dynamics structure factor is calculated with the Chihara formalism[18, 19], given by Equation 4.2. The first term is the elastic scattering feature, which accounts for scattering from electrons that follow the motion of the ions. Screening from the valence electrons is given by $q(k)$, $f_I(k)$ is the ion form factor, which accounts for bound electrons, and $S_{ii}(k,\omega)$ is the ion-ion structure factor. The remaining two terms describe the inelastic scattering feature. The second term describes free-free scattering, where Z_f is the number of free electrons and S^0_{ee} is the electron-electron structure factor. The final term accounts for bound-free scattering, where Z_B is the number of bound electrons, $\tilde{S}_{ce}$ is the structure factor of the core electrons. S_S is the self ion structure factor.

$$S(k,\omega) = |f_I(k) + q(k)|^2 S_{ii}(k,\omega) + Z_f S^0_{ee}(k,\omega) + Z_b \int d\omega' \tilde{S}_{ce}(k,\omega-\omega') S_S(k,\omega') \quad (4.2)$$

The measured spectrum was compared to the theoretical spectra with χ^2 fitting, shown in Figure 4.8 B). We find a solution at T=25±15 eV and Z=2.5±1 shown in Figure. 4.8 A) at 15 ns, and the results of the other shots are plotted in Figure 4.9.

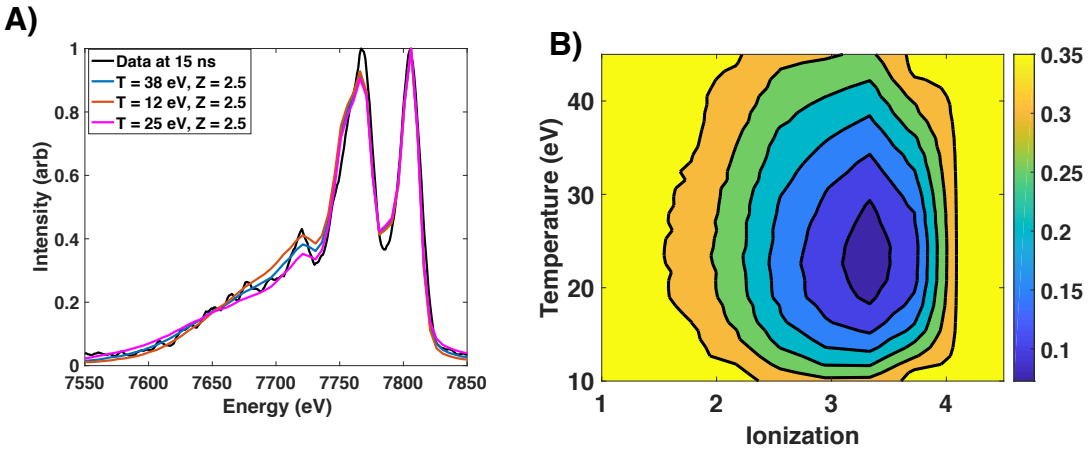

Figure 4.8: A) Measured scattered x-ray spectrum at the shock front compared with theoretical scattering spectra with varying temperatures. B) χ^2 fit between the measured scattered x-ray spectrum and theoretical scattering spectra with varying temperatures and ionizations.

4.4 Comparison to Equation of State Tables

The inferred shock velocity, compression and temperature obtained from the experiment can be compared to Hugoniot calculations of Los Alamos National Laboratory (LANL) SESAME EOS tables for carbon. The pressure of the shocked foam is needed for the comparison, and can be calculated with the Rankine-Hugoniot jump conditions using the measured average shock velocity and inferred compression,

$$p_2 - p_1 = u_1^2 \left(\rho_1 - \frac{\rho_1^2}{\rho_2} \right). \tag{4.3}$$

Here p_1, p_2 are the pressures of the unshocked and the shocked layers, respectively, ρ_1, ρ_2 are the densities of unshocked and the shocked layers, respectively, and u_1 is the shock velocity. The ambient pressure is assumed to be negligible, with $p_1 = 0$.

The uncertainty in the pressure is estimated by the chain rule,

$$\delta P = \sqrt{\left(\frac{\partial P}{\partial \rho_2}\delta\rho_2\right)^2 + \left(\frac{\partial P}{\partial u_1}\delta u_1\right)^2}, \tag{4.4}$$

leading to,

$$\delta P = \sqrt{\left(\frac{u_1^2\rho_1^2}{\rho_2^2}\right)^2 (\delta\rho_2)^2 + \left(2u_1\left(\rho_1 - \frac{\rho_1^2}{\rho_2}\right)\right)^2 (\delta u_1)^2}. \tag{4.5}$$

Here $\delta\rho_2$ is the uncertainty in the density measurement and δu_1 is the uncertainty in the velocity measurement. The uncertainty in the density is found from the ray tracing analysis, and has values of 150 mg/cc for most shots. The uncertainty in the shock velocity is found from fitting a line to the shock front locations, given in Figure 4.7, and has a value of 37 km/s. Note that the relative uncertainties $RU_X = \delta X/X$, for shock velocity $RU_u = 47\%$ and shocked density $RU_\rho = 25\%$ are large.

We compare the inferred compression and temperature of the shocked carbon foam to Hugoniot calculations from three SESAME equation of state tables for carbon. The carbon tables include two graphite tables, SESAME 7832 and SESAME 7833, and a diamond table, SESAME 7834. The Hugoniot is calculated from the carbon tables by iteratively solving the Hugoniot equation,

$$\epsilon_2 - \epsilon_1 = \frac{1}{2}(p_2 + p_1)\left(\frac{1}{\rho_1} - \frac{1}{\rho_2}\right), \tag{4.6}$$

where ϵ is the specific internal energy. The tables are structured such that pressure and internal energy are given as a function of density and temperature. Since equation 4.6 does not explicitly depend on temperature, the calculation is framed as an optimization problem in which the density is chosen such that the corresponding pressure and internal energy best solves Equation 4.6 for a fixed temperature.

The compression calculations for the three carbon SESAME tables are compared to the compression inferred from the experiments in Figure 4.9 A), and the inferred

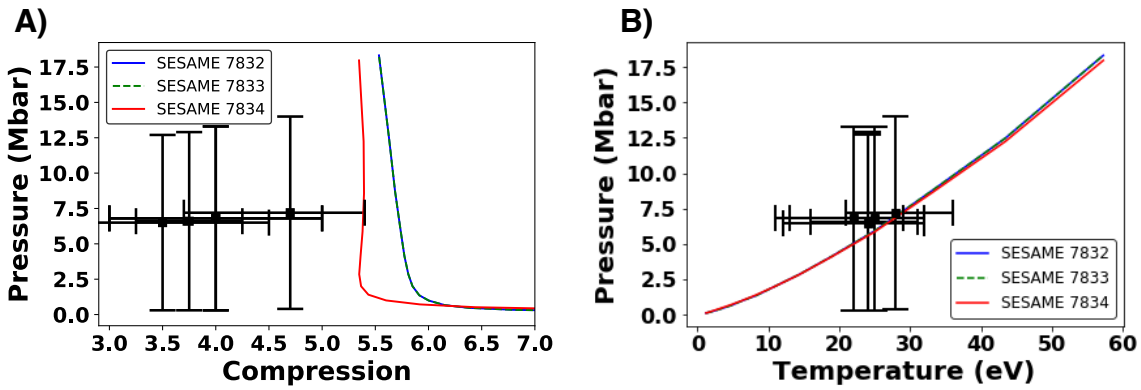

Figure 4.9: A) Comparison of density inferred from the experiments and the calculated Hugoniots of different SESAME tables for carbon. Note that the low pressure (P<1 Mbar) has a compaction phase where the density approaches solid density, and is not shown to better highlight the discrepancy between the data and the Hugoniots predicted from the EOS tables. B) Comparison of temperature measured and the Hugoniots of different SESAME tables for carbon.

temperature measurements are compared to the Hugoniot calculations in Figure 4.9 B). The immediate observation is that the uncertainties in pressure is very large for the experimental data points, which is due to the large uncertainties in the shock velocity and shocked density. Due to the large uncertainty in pressure, shock density and shock velocity, these measurements are not suited for tuning EOS models that go into the EOS tables.

The experimental results do clearly indicate that the inferred compression is smaller than the compression predicted from the carbon EOS tables. A potential explanation for the lower inferred compression is due to heating of the foam upstream of the shock front. Raising the initial temperature in the foam would cause the shock to not be in the strong shock regime. Therefore, a higher upstream temperature would lead to increased post-shock temperatures and lower post-shock density, compared to a lower upstream temperature with the same shock velocity. To illustrate this scenario, Figure 4.10 plots the solutions of the Hugoniot given in Equation 4.6 with varying initial temperatures and using an ideal gas EOS. The adiabatic index was

set to 1.44 to approximately obtain the same compression as the EOS tables at room temperature. The results are more consistent with the inferred compression, however the error bars are large. The heating of the upstream foam could be from the shock itself, as discussed in the next chapter, or from hard x-rays from laser ablation.

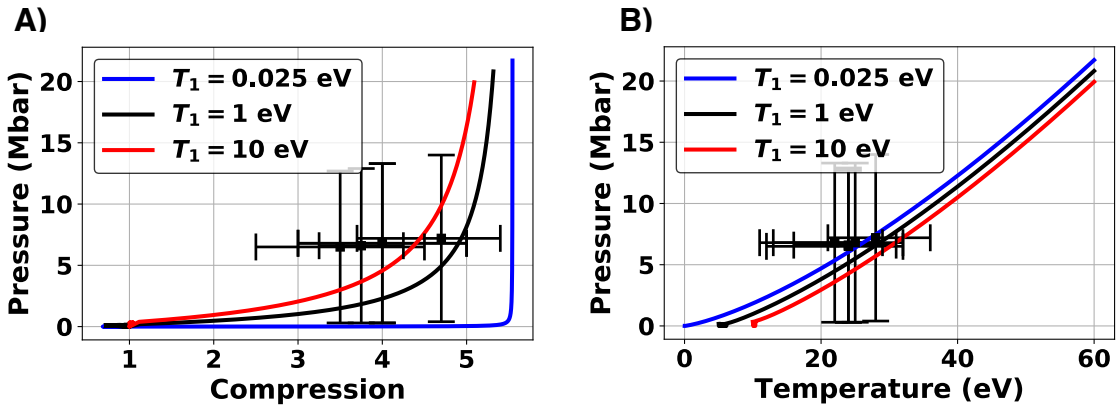

Figure 4.10: Comparison of inferred density in A) and inferred temperature in B) to calculated Hugoniots with different initial temperatures for an ideal gas EOS with $\gamma = 1.44$ different SESAME tables for carbon.

A second potential explanation for the lower inferred compression compared to EOS tables could be due to the ray tracing analysis being performed with a 1-D geometry. The ray tracing analysis includes simulations that were run in 1-D and then extrapolated to 3-D to create a planar shock wave. This method would not account for integrating over any 3-D effects, such as curvature of the shock front, which would lower the inferred compression. The good agreement of the ray tracing analysis over the entire imaged data gives confidence in the current analysis, however we can not rule out the possibility of other geometries that would match the data.

4.5 Conclusion

This chapter reported experimentally inferred temperature, density, and shock velocity of shocked carbon foams using the IXTS diagnostic. Modifications to the platform developed in Chapter 3, including the redesign of the x-ray probe and changing

the foam material from 340 mg/cc RF foam to 150 mg/cc CRF foam. Ray tracing analysis was used to obtain shock velocity and compression for each shot. Unfortunately the analysis resulted in large uncertainties for both inferences. Temperature inferences were obtained by fitting the measured scattered x-ray spectra to theoretical spectra calculated with varying plasma conditions. The results of the temperature and density inferences were compared to Hugoniot calculations for carbon SESAME EOS tables. The large uncertainties in the values makes precise conclusions difficult, however there is a clear discrepancy between the experimentally obtained compression and compression predicted by the SESAME EOS tables which provides motivation for further studies.

CHAPTER V

Void Closure in Shocked, High Porosity Materials

5.1 Introduction

This chapter describes a theory for pore closure in strongly shocked and highly porous materials. Previous work on modeling void closure in shocked porous materials has mainly focused on pore collapse models, which describe the relation between the equation of state of the solid density material to a porous material by a compaction relation. The most common pore collapse model used is the P-α model [41, 16], where the compaction relation is used to model the crushing of the pores up to a critical crush pressure, at witch the voids are completely closed.

The present work is focused on shocks that are much stronger than the compaction pressure of the porous material, and on highly porous materials where the density is far bellow the solid density. We conceptualize a scenario where thermal radiation from the shocked material can substantially heat the highly porous upstream material, causing the voids to close from thermal expansion. We develop a simple 1-D model based on conservation of energy to estimate the heating of the porous material ahead of the shock. The thermal radiation from the shock is able to penetrate deep into the mostly vacuum, upstream material, leading to appreciable heating. Due to the extent of which the radiation can penetrate, there may be sufficient time for the pore walls to thermally expand and close before the shock reaches the void. Both the heating

and the void closure imply that traditional approaches to modeling the Equation of State of these materials may produce incorrect results.

This work is divided into two main parts. First, we will develop a model to estimate the temperature of the pore walls upstream of the shock. Next we will compare timescales of the shock transit time to a simplified void wall expansion time to assess the feasibility of pore closure. Results for carbon foam will be shown. We then consider the role of electron heat transport in pore heating and closure, and then the implications of our results for EOS calculations.

5.2 1-D Model for Calculating the Upstream Temperature

The goal of this section is to estimate the heating upstream of the shock for independent variables porosity, ϕ, and shock velocity, u_s. Porosity was chosen to classify the how porous a material is because it is a macroscopic variable that is independent of material composition and manufacturing process. The porosity is also commonly known experimentally. The shock velocity is one of a few parameters that could be used to characterize the strength of the shock. Shock velocity was chosen as it is a commonly measured experimentally in both HEDP experiments and equation of state measurements. The first subsection will describe the geometry and porosity in further detail and the second subsection will set up the heating model. After that, we compare the thermal radiation flux to a thermal electron flux.

5.2.1 Geometry and Porosity

Porosity is defined as the ratio of void volume space to total volume space, given by

$$\phi = \frac{V_V}{V_T} = 1 - \frac{\rho_{\text{average}}}{\rho_{\text{solid}}} = 1 - \frac{1}{\alpha}. \tag{5.1}$$

Where V_V is the volume of the voids, V_T is the total volume, ρ_{average} is the average density of the porous material, ρ_{solid} is the solid density of the porous material. It is also useful to define a distention parameter $\alpha = \frac{\rho_{\text{solid}}}{\rho_{\text{average}}}$. Note that with this definition, $0 \leq \phi \leq 1$ and $\alpha \geq 1$.

To roughly define the region of high porosity of interest to this work, we consider upper and lower limits. For the lower limit on high porosity, we will consider an idealized model of a porous material with spherical voids of constant size that do not overlap and find the most efficient way to maximize the porosity. This model is directly analogous to the well known efficient hard sphere packing problem, where the goal is to minimize the space between solid spheres of a fixed size. The limit in efficiently packing hard spheres[36] corresponds to a $\phi \approx 0.74$. Going past this limit corresponds to breaking some of the assumptions namely shape (spherical voids), uniform void size, and non-overlapping voids (hard spheres). Indeed when we look at the structure of high porosity foams they are often open-celled structures with a wide range of pore geometries. We define high porosity for this work as $\phi \gtrsim 0.74$. For a CH foam of solid density of 1 g/cc, this corresponds to foams densities $\lesssim 0.26$ g/cc. While there is ongoing work to create an ultra-low porosity foams[84], we consider a practical upper limit of $\phi \approx 0.999$, which corresponds to plastic foam density of 1 mg/cc.

Porosity is a good classifier of porous materials on a macroscopic scale, but it does not give any information on how an individual pore is structured. For our problem we are interested determining the scaling of the amount of mass the radiation encounters as a function of porosity. Our approach is to use a combination of conservation of mass and the definition of porosity to model an individual 1-D, representative pore and then to stack the individual pores in 1-D to represent the macroscopic porous material.

A schematic of the representative pore is given by figure 5.1. The size of the

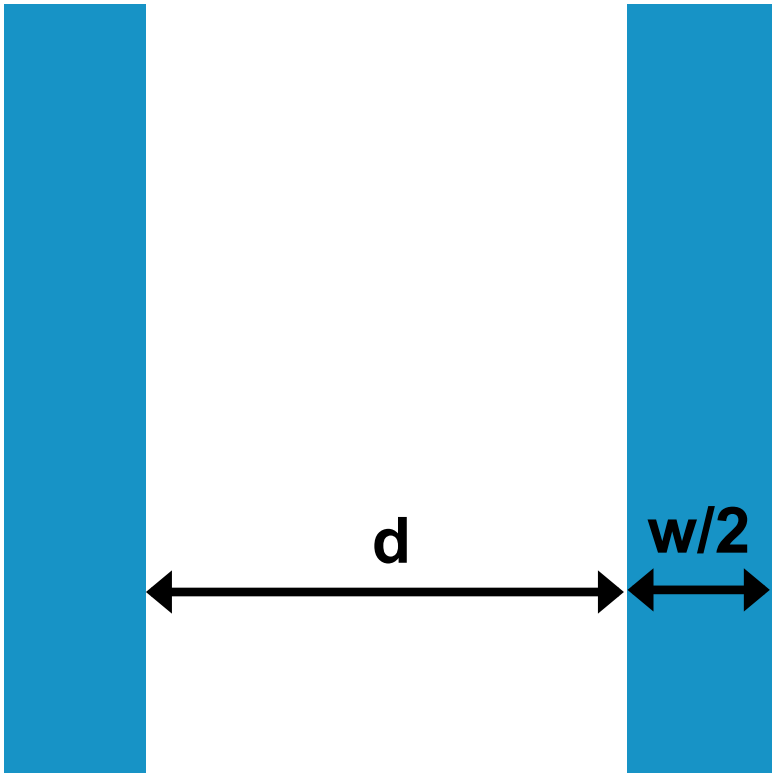

Figure 5.1: A schematic of the representation of an individual pore. The blue region represents solid density pore walls with width $w/2$, and the vacuum pore has pore length d.

pore is set by a given characteristic void length d, which we set to be 100 nm. The representative pore is modeled as 1-D planes with infinite extent in the remaining two dimensions to correctly conserve mass and so that the pore wall thickness w can have a straightforward handling in 1-D. With reference to Figure 5.1, we define the total 1-D volume as $V_T = d + 2(\frac{w}{2})$ and the 1-D void volume as $V_V = d$. Inserting the geometry relations into Equation 5.1 gives,

$$\phi = \frac{V_V}{V_T} = \frac{d}{d+w}. \tag{5.2}$$

The scaling of the pore wall width with porosity can then be found by rearranging Equation 5.2, yielding

$$w(\phi) = d(\phi^{-1} - 1). \tag{5.3}$$

With the individual pores defined, we can stack them in 1-D and complete the geometry of the problem, as illustrated in Figure 5.2. Note that the stacking of pores still conserves the original porosity, as can be demonstrated by by considering a geometry of n pores. The total porosity then is $\phi' = \frac{nV_v}{nV_T} = \frac{V_v}{V_T} = \phi$.

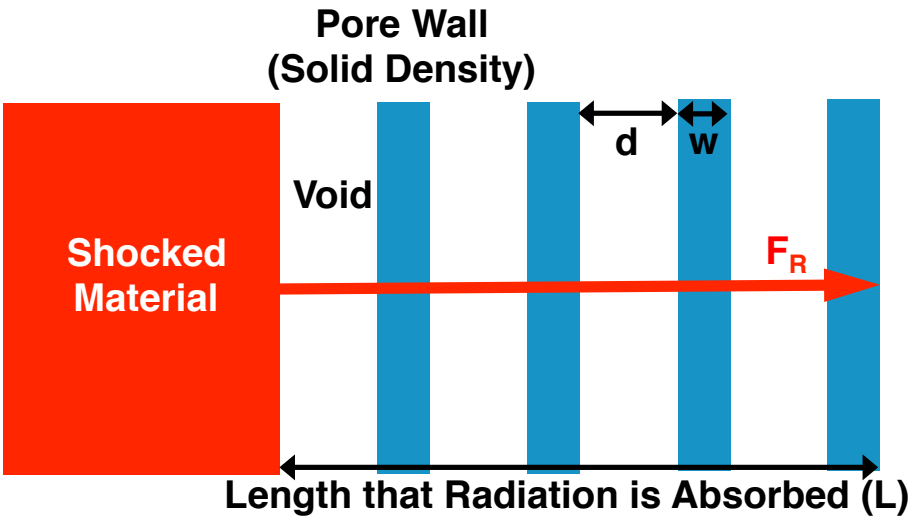

Figure 5.2: A schematic of the full geometry of the problem. The porous material upstream of the shock (red) is constituted of individual pores represented by Figure 5.1 (blue). The radiation energy flux from the shocked material (F_R) penetrates a depth of L and heats the upstream pore walls.

5.2.2 Upstream Heating Model

The conservation of energy equation is used as a starting point to develop a model for the upstream heating of porous material model. We take the point of view that the radiation penetrates upstream supersonically, ahead of the density jump produced by the shock. This is characteristic of radiative precursors. In this case, the energy equation reduces to

$$\frac{\mathrm{d}(\rho_s \epsilon)}{\mathrm{d}t} = \nabla \cdot \mathbf{F}_R, \tag{5.4}$$

where ρ_s, is the (solid) density of the pore wall, ϵ is the specific internal energy and $\mathbf{F}_R$ is the radiation energy flux. In order to calculate the pore heating before the shock

wave arrives, we assume that the density of the pore wall does not change, so that we need not account for the density dependence of the opacity. Later we will estimate a pore closure time, assuming the pore walls can expand. The assumptions in these two calculations are not consistent, but will serve here to obtain a first estimate of the regimes of behavior and their boundaries. Similarly, in the 1D case calculated here, the radiation flux corresponds to a beamlike angular distribution, while in 3D the angular distribution transitions from Lambertian toward beamlike as one moves further ahead of the shock. Noting that $\mathrm{d}\epsilon = c_V \mathrm{d}T_p$, where T_p is the temperature of the pore wall and c_V is the specific heat capacity at constant volume, gives

$$\rho_s c_V \frac{\mathrm{d}T_p}{\mathrm{d}t} = \frac{\mathrm{d}F_R}{\mathrm{d}x}. \tag{5.5}$$

Here we have assumed that the heat capacity does not change with the temperature. As a heuristic, we will assume that the heating occurs uniformly to a depth at which the thickness of pore-wall material penetrated equals one radiation mean free path, λ, and is negligible beyond that. With this heuristic $\frac{\mathrm{d}F_R}{\mathrm{d}x} = \frac{F_R}{\lambda}$. We then use Equation 5.5 to obtain an expression for the temperature increase of the pore wall, ΔT_p over an upstream heating time scale δt, as

$$\Delta T_p = \frac{F_R}{\rho_s c_V \lambda} \delta t. \tag{5.6}$$

The amount of time available for heating is given by the total absorption length for the radiation, including both vacuum regions and walls, divided by the shock velocity. Note that this is larger than just the mean free path through the solid pore walls, since the radiation is not attenuated through the vacuous pores. This is illustrated by the length scale L in Figure 5.2. The time scale then is

$$\delta t = \frac{n(w+d)}{u_s}, \tag{5.7}$$

where w is the width of the pore wall, d is the length of the pore and n is the integer number of pores penetrated. The number of pores can be found by

$$n = \text{ceiling}\left[\frac{\lambda}{w}\right]. \tag{5.8}$$

Finally, using $\lambda \approx nw$ and assuming that the initial upstream temperature is negligible,

$$T_p = \frac{F_R}{\rho_s c_V u_s}\frac{(d+w)}{w}. \tag{5.9}$$

The geometric terms d and w were addressed in the previous section, so this leaves the radiation energy flux and the heat capacity. To estimate the radiation energy flux F_R, we assume that the shocked and upstream material are optically thick. This allows us to treat the radiation of the shock as a blackbody emitter and allows us to say that the radiation is completely contained in the upstream material. The net radiation energy flux is the difference between the radiation flux moving upstream from the shock-heated material and that moving downstream from the heated material in the precursor. We approximate this as,

$$F_R = \sigma(T_s^4 - T_p^4). \tag{5.10}$$

Here T_s is the brightness temperature of the radiation from the shocked material and σ is the Stefan-Boltzmann constant.

There are two regimes considered in this work that will influence the value of T_s. There are differences in the structure, and therefore the post shock temperature, of the shocked material. The first regime corresponds to the limit where the radiation energy flux is insignificant compared to the incoming material energy flux. A relevant parameter is the ratio of the radiation energy flux leaving the shock to the incoming material energy flux, $\xi = \frac{2\sigma T_s^4}{\rho_0 u_s^3}$. Since there are no other energy sources in this

system, the energy available to radiate is limited to some fraction of the incoming material energy. The maximum value is $\xi = 0.7$ in the optically thick upstream and downstream case [25].The second regime is when the shock becomes sufficiently strong and the structure is dominated by radiation. The transition between the two regimes is quite rapid, as in the non-radiative regime $\xi \propto u_s^5$. We assume here that the transition is instantaneous.

For small ξ, the temperature is given by the usual jump conditions for the non-radiative regime. To express the shock temperature as a function of shock velocity u_s, we will assume the upstream and shocked matter is an ideal gas with an adiabatic gas constant γ. The temperature produced by a strong shock is then given by

$$T_s = \frac{2Am_p}{k_B(Z+1)} \frac{(\gamma-1)}{(\gamma+1)^2} u_s^2. \tag{5.11}$$

Here k_B is the Boltzmann constant, Am_p is the approximate atomic mass in kg, and Z is the ionization.

The heat capacity is the last parameter needed to solve Equation 5.9 and find the wall temperature when the shock reaches a given pore, T_p. We assume that the upstream material is a fully ionized (Z=6 for carbon), ideal gas to be consistent with assuming that the heat capacity does not depend on temperature. One has,

$$c_V = \frac{n}{2} \frac{(Z+1)k_B}{Am_p}, \tag{5.12}$$

which gives a value of 6.7×10^3 J/K. The assumption of a fully ionized plasma for the pore walls will likely overestimate and underestimate the heat capacity for certain pore wall temperature regions due to a combination of the pore wall being only partially ionized and neglecting ionization effects in formulating the heat capacity. The value of c_V will be accurate to better than a factor of two once the pore walls reach temperatures of about 10 eV.

Combining Equations 5.9 and 5.10 gives the final expression for the temperature of the pore walls,

$$\sigma T_p^4 + T_p = \frac{\sigma T_s^4}{\rho_s c_V u_s} \frac{(d+w)}{w}. \tag{5.13}$$

This equation was solved using the fsolve algorithm in the SciPy [49] library.

The results of Equation 5.13 are shown in Figure 5.3. Here we use values for a carbon porous material (foam), which include for the soild density $\rho_s = 2.2$ g/cc, specific heat capacity at constant volume $c_V = 6.7 \times 10^3$ J/K, and adiabatic constant $\gamma = 5/3$.

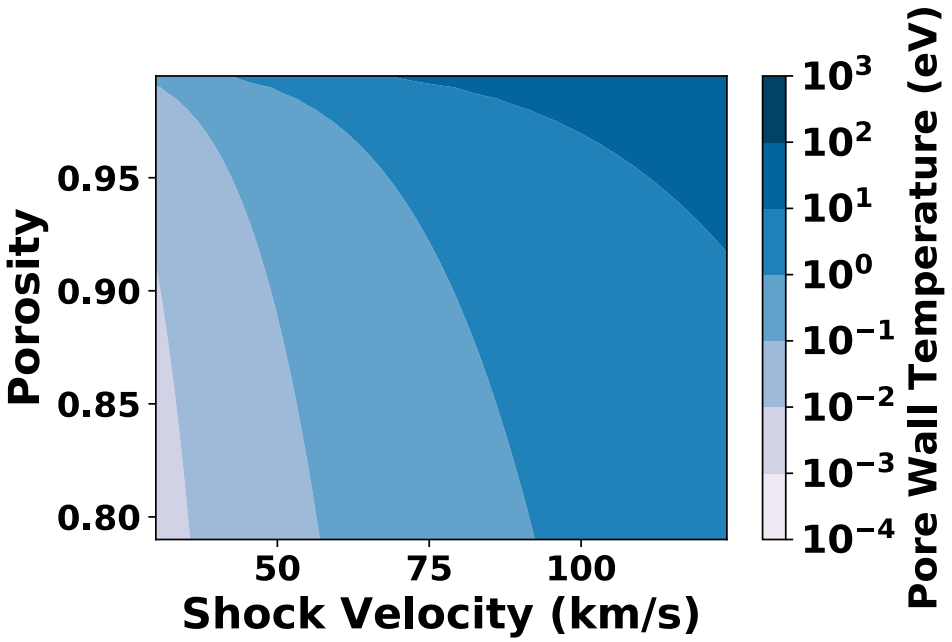

Figure 5.3: Solution for the pore wall temperature T_p from Equation 5.13. The solution was found assuming a carbon porous material, with solid density of 2.2 g/cc.

Figure 5.4 A) and B) plot the solutions, as a function of shock velocity, for $\phi =$ 0.8, 0.9, 0.98, and 0.99, which represent porosities on the lower end of 'high porosity' as well as higher porosities. The general trend is that the upstream pore wall temperature increases with increasing porosity and shock velocity. The model generally

estimates pore wall temperatures of under a few eV for lower porosity and/or lower shock velocity systems, tens of eV for high porosity materials and tens of km shock velocities, and potentially greater than 100 eV for very high porosity materials and shock velocities greater than 100 km/s.

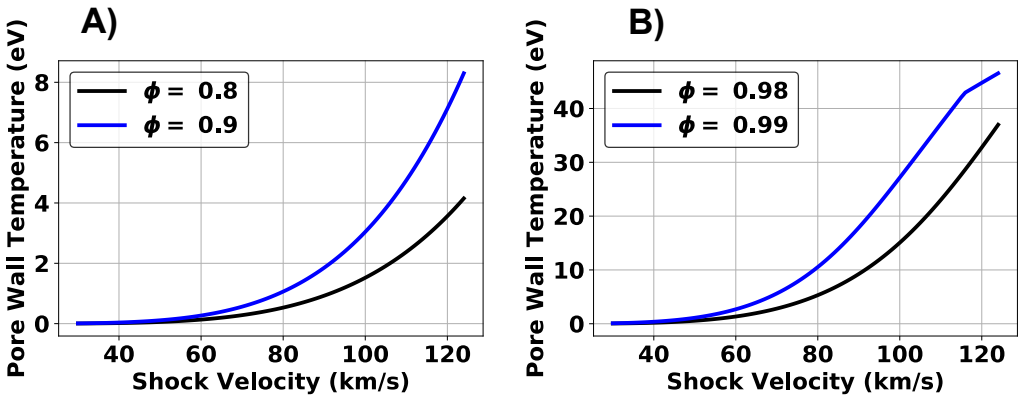

Figure 5.4: Lineouts for specific porosity values from Figure 5.3. A) Corresponds to the lower end of 'high porosity', where porosities of 0.8 and 0.9 corresponds to average foam densities of 440 mg/cc and 220 mg/cc respectfully. B) Corresponds to a range of high porosity foams commonly used in HEDP targets, where porosities of 0.98 and 0.99 corresponds to average foam densities of 44 mg/cc and 22 mg/cc respectfully.

5.2.3 Comparison to Thermal Electron Flux

The previous subsection showed that appreciable heating upstream of the shock can occur from the thermal radiation from the shocked material. There are other potential sources of energy that could contribute to the heating of upstream material as well. One possible example is heating due to a free-streaming, thermal electron flux. As the shock is propagating though the porous material, the shock front will encounter vacuous pores. The thermal electrons, which have greater velocity than the shock front, may be able to stream freely through the vacuum pores and heat the opposing wall before the shock arrives. The free-streaming, thermal electron flux, F_e, is defined as

$$F_e = f n_e k_B T_e v_{the}, \tag{5.14}$$

where f is a flux limiter, n_e is the electron density, k_B is the Boltzmann constant, T_e is the electron temperature, and v_{the} is the thermal electron velocity.

A rough estimate to determine the potential for heating is to compare the free-streaming, thermal electron flux to the thermal radiation flux. We define this ratio as

$$\Upsilon = \frac{F_e}{F_R} = \frac{f n_e k_B T_e v_{the}}{\sigma T_s^4}. \tag{5.15}$$

This is likely to be a conservative comparison due to implicitly assuming that the mean free paths are the same. For heating from the free-streaming, thermal electrons to be appreciable, we expect that the free-streaming, thermal electron flux to at a minimum be comparable to the radiation flux, or $\Upsilon \geq 1$. Figure 5.5 shows the result of Equation 5.15, assuming that the shocked material is fully ionized (Z=6) and that $f = 0.4$.

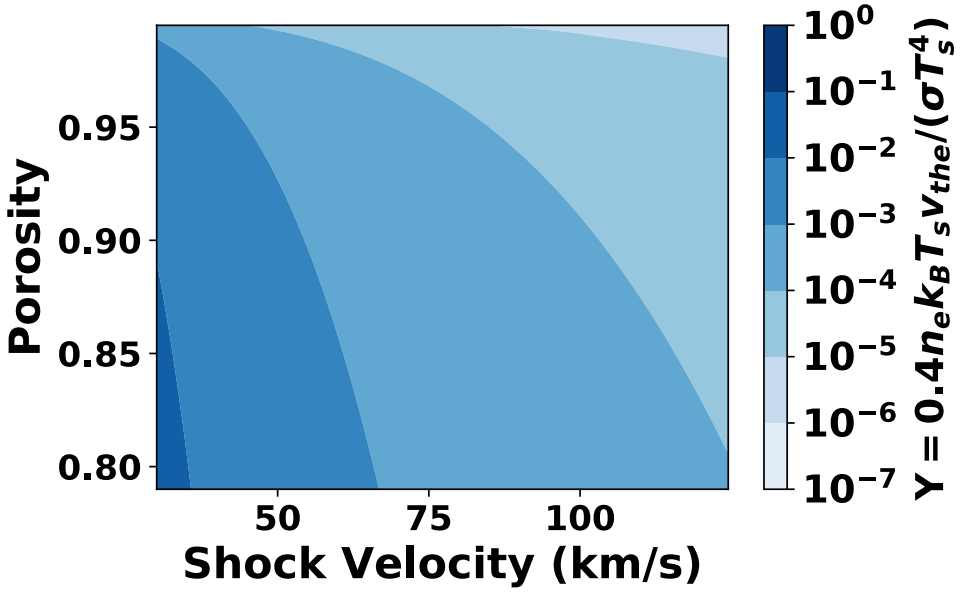

Figure 5.5: Solution for the flux ratio Υ from Equation 5.15. The solution was found assuming that the shocked material is fully ionized and the the flux limiter $f = 0.4$.

From Figure 5.5, we conclude that heating due to free-streaming electrons is insignificant compared to the heating due to thermal photons. To investigate this

further, we will assume that the electron temperature is equal to the brightness temperature and noting that $v_{the} \propto T_e^{\frac{1}{2}}$, gives $\Upsilon \propto T_e^{-5/2} \propto u_s^{-5}$. Due to the strong scaling with the shock temperature, only at low shock velocities could the free-streaming, thermal electron flux be comparable to the thermal electron flux. However, at such low shock velocities, the electrons are not energetic enough to cause appreciable heating upstream.

5.3 Estimating Pore Closure

The results of the previous section suggests that radiative heating may produce appreciable temperatures upstream of the shock in the precursor region under conditions of interest for present-day experiments. Given these conditions, we are now interested in seeing if there is sufficient time for the pore walls to expand and fill in the voids prior to the arrival of the shock. We approach this problem by comparing the time it takes for the shock to traverse the entire length of the precursor region, which is given by Equation 5.7, to the time it takes for the heated pore walls to expand into the vacuum pores. From this comparison we will find the maximum pore size that could close during this time. This simple, 1D model cannot account for more complex consequences of actual pore geometries, such as the generation of vorticity from the interaction of the expanding plasmas. What the present calculation can show is the approximate regimes over which pore closure may occur.

To calculate the number of pores penetrated in equation 5.7, we need to determine the mean free path of the thermal radiation through the upstream material. To approach this we used PropacEOS to calculate the Planck mean opacity for solid density carbon at temperatures corresponding to the pore wall temperature, given by Figure 5.6 A). We estimate the mean free path as $\lambda = 1/\alpha$, where α is the opacity averaged over the thermal radiation Planckian spectrum corresponding to the brightness temperature of the emission from the shock front, T_s. The results are

shown in Figure 5.6 B).

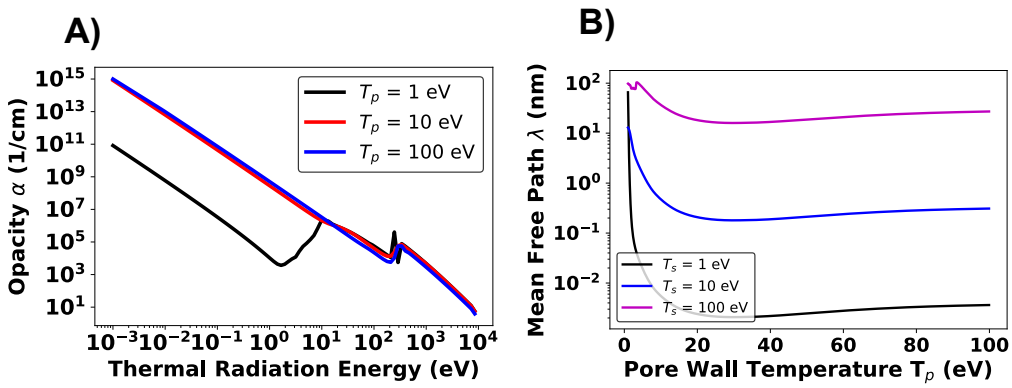

Figure 5.6: A) The opacity for carbon at solid density calculated from PropacEOS for pore wall temperatures T_p of 1 eV (black), 10 eV (red) and 100 eV (blue). B) The averaged mean free path through solid density carbon as a function of pore wall temperature T_p for thermal radiation of temperatures T_s of 1 eV (black), 10 eV (blue) and 100 eV (purple).

The timescale for the pores to close is given by $\tau_c = \frac{l}{2c_T}$, where l is the maximum pore size and c_T is the isothermal sound speed, given by $c_T = [(1+Z)k_B T_c/Am_p]^{\frac{1}{2}}$. Here T_c is a characteristic temperature. In reality, the temperature of the expanding material will increase with time as the shock approaches the pore. Here, we assume that the characteristic temperature is half of the final temperature in the pore wall. We then find the maximum pore size that will close before the shock arrives by equating the two time scales, which leads to

$$l = 2n(w+d)\frac{c_T}{u_s}. \tag{5.16}$$

The results of Equation 5.16 are shown in Figure 5.7. The general behavior is that the maximum size of a pore that closes increases with increasing porosity and increasing shock velocity. Figure 5.8 A) gives the results of Equation 5.16 for $\phi = 0.8$ and 0.9, which represents the lower end of the porosity range considered in the work. Results of Equation 5.16 for porosities of 0.98 and 0.99 are given in Figure 5.8 B). For both cases there is noticeable structure, which is due to structure in the opacity

of carbon and will change for different materials. The maximum pore size that has sufficient time to close ranges from tens of nm for lower porosities to hundreds of nm for high porosity. This agrees well with typical pore sizes seen in foams[66], indicating that pore closure ahead of the shock in HEDP experiments is often likely.

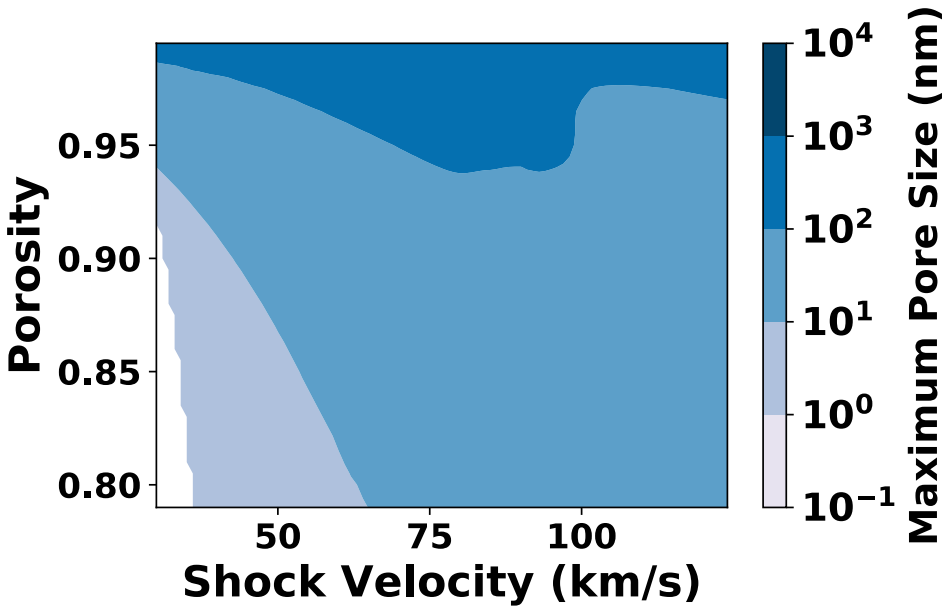

Figure 5.7: Maximum pore sizes that have sufficient time to close during the shock transit time as a function of shock velocity and porosity, calculated from equation 5.16.

5.4 Implications for Equations of State and Modeling

Having concluded that foam materials in present-day HEDP experiments often will be heated ahead of shock waves, we now discuss the implications of this for EOS models and simulations. The major effect seen here relates to opacities and heating. The structure in the foam leads to heating that differs from that of a uniform medium, such as a gas, for two reasons. First, there are geometric effects due to the foam having structure that occur in the heating model. Second, the opacity of the foam, which is composed of solid density material and voids, differs from that of a uniform gas of the same material and average density.

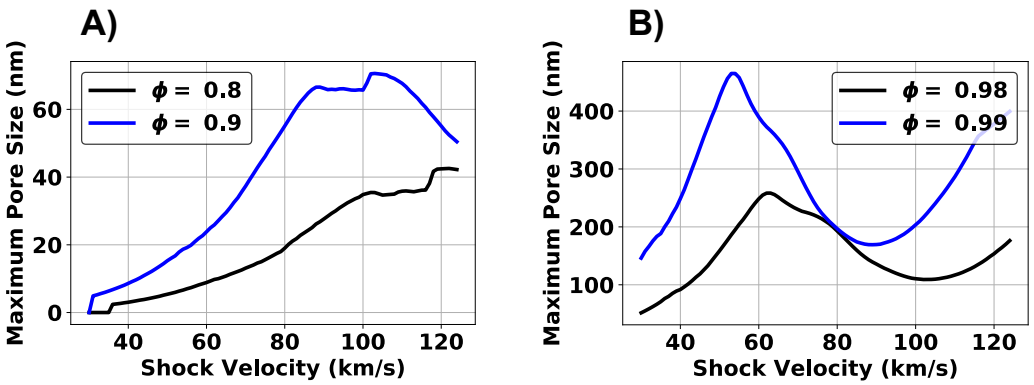

Figure 5.8: Lineouts of the maximum size of a pore that will close for specific porosity values from Figure 5.8. A) Corresponds to the lower end of 'high porosity', where porosities of 0.8 and 0.9 corresponds to average foam densities of 440 mg/cc and 220 mg/cc respectfully. B) Corresponds to a range of high porosity foams commonly used in HEDP targets, where porosities of 0.98 and 0.99 corresponds to average foam densities of 44 mg/cc and 22 mg/cc respectfully.

We first reformulate the geometry developed in Section 1 to generalize to m dimensions to highlight the geometric effects. Referring to Figure 5.1, the representative pore geometry is abstracted as an m-dimensional cube. This leads Equation 5.2 to generalize to $\phi = d^m/(d+w)^m$. Solving for w gives,

$$w = d(\phi^{-1/m} - 1). \tag{5.17}$$

With the generalized geometry defined, we are now interested in comparing the upstream heating of a porous material to that of a uniform gas. We assume that the foam has the same average density as the gas, or $\rho_p = \rho_g$, where ρ_g is the density of the gas. The heating model for a gas can be found by starting at Equation 5.6, and using the gas density in place of the solid density. The timescale for heating in the gas is then $\delta t = \lambda_g/u_s$, where λ_g is the mean free path of the gas. Inserting in δt and noting that $F_R = \sigma T_s^4 - \sigma T_g^4$ gives

$$\sigma T_g^4 + T_g = \frac{\sigma T_s^4}{\rho_g c_V u_s}, \tag{5.18}$$

where T_g is the temperature of the upstream gas. With the heating model for a uniform gas developed, we now compare it the heating model of the porous material. We define the ratio of these two models with the same shock conditions as

$$\chi = \frac{\sigma T_p^4 + T_p}{\sigma T_g^4 + T_g} = \frac{\rho_g}{\rho_s}\frac{(d+w)}{d}, \tag{5.19}$$

where we have assumed that the heat capacities are the same. Noting that $\rho_g = \rho_p$, then $\rho_g = \rho_s(1-\phi)$ from Equation 5.1. Plugging in the generalized expression for w into Equation 5.19, gives

$$\chi = \frac{1-\phi}{1-\phi^{1/m}}. \tag{5.20}$$

Note that for high porosities, Equation 5.20 approaches the dimension parameter, or

$$\lim_{\phi \to 1} \chi = m. \tag{5.21}$$

This result suggests that A) the upstream temperature of a porous material is equal to or larger than that of a uniform gas, and that B) this difference may depended on the geometry of the simulation.

Next we will investigate the opacity differences between a foam and a uniform gas with the same average density and temperature. In particular, we will explore the conditions where the pore walls have likely not closed, resulting in the porous material still being composed of solid density material with vacuum voids dispersed throughout.

To explore this, we define an effective mean free path that the photons travels through the porous material, including vacuum and solid density as,

$$\lambda_p = n(d+w) = \frac{d+w}{w}\lambda_s. \tag{5.22}$$

Here λ_p is the mean free path of the porous material and λ_s is the mean free path of

the solid-density pore walls. Inserting Equation 5.17 into Equation 5.22 gives

$$\lambda_p = \frac{1}{1-\phi^{1/m}}\lambda_s. \tag{5.23}$$

With the mean free path of the porous material expressed in terms of porosity and solid-density mean free path, we are now interested in comparing the mean free path of the porous material to that of a gas. To evaluate this analytically, we will consider a limiting case where the absorption is dominated by inverse bremsstrahlung. A simple expression for the mean free path in this case is given by Drake [25] on page 269, where the mean free path relation on density is $\lambda \propto 1/\rho^2$. Using this expression, the ratio then becomes,

$$\Psi = \frac{\lambda_p}{\lambda_g} = \frac{\rho_g^2}{\rho_s^2}\frac{1}{(1-\phi^{1/m})}. \tag{5.24}$$

Noting that the average densities are the same, $\rho_g = \rho_p$, gives $\rho_g = \rho_s(1-\phi)$. Inserting this expression into 5.24 gives

$$\Psi = \frac{(1-\phi)^2}{(1-\phi^{1/m})}. \tag{5.25}$$

The solution to Equation 5.25 is given in Figure 5.9 for m=1,2,3 dimensions. While the mean free path ratio is above 1 for low porosities, for high porosities the ratio is significantly below 1. These results suggest that modeling of the behavior of porous foams could be improved by adjusting the opacity model for conditions in which the pores have likely not closed. In effect one should increase the opacities by some factor dependent on the geometry of the problem for temperatures below those necessary to quickly dissolve the solid walls.

One might designate the regime we have explored as the "heating regime" for porous materials, in contrast to the "crushing regime" discussed in the introduction of this chapter and in Chapter 2. In the crushing regime, the relation of pressure and

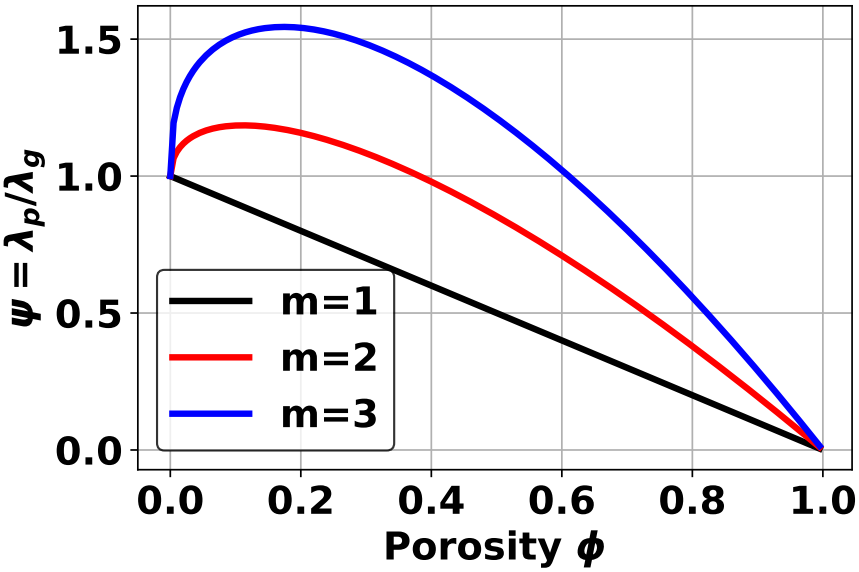

Figure 5.9: Ratio of the mean free path of a porous material to the mean free path of a gas with the same average density as a function porosity and dimension m.

internal energy is strongly affected by the internal structure. In the heating regime, in contrast, the pressure, internal energy, and ionization will be determined primarily by the amount of heat absorbed in the matter. There will be some secondary effects. As the pores close, turbulent flow may alter these relationships for some period of time [40]. In addition, during some periods of time the foam material will include both solid matter and gas or plasma, leading to differences in EOS quantities. These secondary effects are transient, however, and so cannot be treated within the context of equilibrium EOS models. Existing EOS tables likely do as well as one can regarding the pressure, internal energy, and ionization of the material.

5.5 Conclusion

This chapter describes a simple 1-D model to estimate the heating of a highly porous upstream material due to thermal radiation from a shock. This model suggest that the material upstream of the shock reaches temperatures of $\gtrapprox$ 1-10 eV for shock

velocities $\gtrapprox$ 75 km/s, which are common in HEDP experiments. A simple thermal expansion model was used to estimate the maximum pore size that could close during the the time it takes for the shock to transit the entire precursor length. This model predicts pore sizes in the range of tens to hundreds of nm can close, which is similar to the characteristic void sizes of many foams used in experiments.

These results could have implications for measuring the equation of state of shocked foams. For example, there are limited viable ways to measure the shock temperature, and streaked optical pyrometry (SOP) is a popular choice. For the conditions assumed in our model, mainly an upstream material that is optically thick, the SOP diagnostic would only measure signal when the precursor reaches the end of the foam. When this breakout occurs, the diagnostic would observe thermal radiation from both the precursor and from the shock front. This would lead to a higher measured brightness temperature in the precursor region.

This work may also impact hydrodynamic instability experiments under HEDP conditions, which are often used to benchmark simulation codes. These experiments typically use tiny, precision-machined perturbations and the upstream material is assumed to be known. Depending on the timing of the experiment, the upstream material could be significantly heated, leading to uncertain initial conditions. Due to the deep penetration of the thermal radiation, there may be sufficient time for the machined perturbations to deform and be less predictable.

CHAPTER VI

Conclusions and Future Directions

This dissertation presented experimental and theoretical work regarding shocked and highly porous materials. Porous materials, foams in particular, are commonly used in high-energy-density physics (HEDP) experiments including hydrodynamics at HEDP conditions, inertial confinement fusion research, and stockpile stewardship research. Simulating these experiments with hydrodynamics codes can be challenging due to the heterogeneous aspect of foams and sparse equation of state (EOS) measurements. This dissertation details two experiments to measure the thermodynamic properties of shocked foams, and a simple 1-D model to propose a new mechanism for pore closure in strongly shocked, high porosity materials.

Chapter 3 presented an experiment on the OMEGA EP laser system dedicated to developing a platform to study shocked foams with the imaging x-ray Thomson spectrometer (IXTS). The challenge of this experiment was overcoming steep geometry restrictions imposed by the facility and the diagnostic. The imaging component of the IXTS data was analyzed with ray tracing analysis to infer a density measurement of the shocked foam and shock front location. The shot front location was plotted against the probe time to obtain a fit for an averaged shock velocity. The scattering spectrum at the shock front was also analyzed, although poor signal and weak heating prevented a precise temperature inference. This experiment was the first time that

the IXTS was fielded on OMEGA EP, and demonstrated the ability to make x-ray Thomson scattering measurements with the restrictive geometry.

Chapter 4 details an experiment on the OMEGA EP laser system that altered the design of the platform developed in Chapter 3. The foam was changed to carbon foam and the density was lowered to 150 mg/cc to drive a stronger shock into the foam and lessen the attenuation of the x-ray probe. The x-ray probe was redesigned to achieve greater laser intensity on target to boost the conversion of laser energy into x-rays, and reduced the pulse length to minimize motion blurring. The experiment inferred compression and temperature for five probe times, and an averaged shock velocity was obtained. The temperature and compression were compared to Hugoniot calculations of commonly used LANL SESAME EOS tables for carbon. Due to the large uncertainties in the inferences, the experimental data is not useful for tuning EOS models. The compression inference, even with the large uncertainties, was distinctly lower than the predictions from the SESAME EOS tables. Better agreement was achieved by changing the initial temperature in the Hugoniot calculations to around ten eV. The pore heating model, discussed in Chapter 5, predicts upstream heating of 5 to 10 eV, which is consistent with the increased initial temperature in the Hugoniot calculations. These results urge caution when using EOS tables to simulate similar experiments, and further motivate the continued study of shocked foams.

Chapter 5 describes a theory for pore closure of strongly shock and highly porous materials. Previous theories are mostly centered on low pressures where the pores are crushed by the shock. This work conceives of a mechanism where thermal radiation from the shocked material can penetrate deep into the mostly vacuum upstream porous material. The walls of the porous material heat from this penetrating radiation and expand to fill in the pores before the arrival of the shock. A simple 1-D heating model was developed based on the conservation of energy to calculate the heating of the pore wall. A simple 1-D thermal expansion model was then used to estimate the

pore closure, and found that the pores may have enough time to close for conditions accessible to HEDP experiments.

6.1 Future Directions

There are numerous potential possibilities for expanding the experimental and theoretical work of this dissertation, and bellow I outline a few candidates for both the experimental and theoretical work.

The geometry of the experimental platform could be changed to accommodate different materials and to obtain better measurements. The main challenge with making an IXTS measurement on OMEGA EP is the restrictive geometry limitations imposed by the facility and the diagnostic. We will assume that reengineering the laser beam paths to allow for different pump-probe geometries is not feasible, which leaves modifications to the IXTS design. The IXTS is currently approved for one diagnostic port due to the design potentially interfering with the laser beams in other diagnostic ports. An IXTS redesigned for OMEGA EP in particular may allow for different ports to be used, which would expand the potential experimental geometries. The IXTS also currently has one crystal in the 8 keV energy range. Crystals for different energy ranges, such as 4.7 keV for the titanium He-α would further increase experimental possibilities.

The experimental platform could also be modified to use additional diagnostics. The IXTS imposes significant challenges to using additional diagnostics, mainly with the vast and carefully designed shielding to protect the low signal data, and the challenge of creating enough x-rays to obtain a significant signal. The author has performed, or been apart of collaborations, to incorporate IXTS measurements with radiography, VISAR, and X-ray fluorescence measurements. These combined techniques have shown some promise, but can have substantial limitations. For example, the 7.8 keV x-ray energy is too high to obtain good contrast with radiography in

low-density foams. Generating a two-color x-ray probe by irradiating two different metals could be an option, however this reduces the 7.8 keV x-ray probe in an already photon starved measurement. The combined VISAR technique is generally limited to optically transparent foams, and the combined X-ray fluorescence technique is either restricted to a suitable fluorescing material, or the foam needs to be doped. A small next iteration could be to include streaked optical pyrometry (SOP) to observe the shock breakout time of a foam target. This could help constrain the shock velocity measurement, which contributed to significant uncertainty in the pressure calculation in Chapter 4.

The final modification could be to the opacity of the foam. The strength of the IXTS measurement generally falls onto a spectrum of the measurement being dominated by the elastic scattering, which is proportional to density, down to being dominated by the attenuation of the x-ray probe, which depends exponentially on density. A middle ground condition might be obtainable where the shocked foam heavily attenuates the x-ray probe, and the unshocked region does not. This might provide significant contrast to the imaging measurement such that ray tracing analysis can more accurately find the shock front and estimate the compression. Increasing the density may achieve this middle ground, as well as using a metal foam, such as a copper foam.

The theoretical pore heating model has many potential improvements. The first is that this work was developed in 1-D to create a simple model to illustrate the heating effect. The model could be improved to treat the radiation transport and pore structure in a 2-D/3-D manner to account for any geometric reduction of the flux. The second improvement would be to treat the heat capacity and ionization of the pore wall as a function of temperature. The current model treats the pore wall as a fully ionized plasma, however a better approach would be to adjust the ionization and heat capacity as the wall heats up.

The model could also be reformulated for different circumstances. For example, the model could be reformulated to solve for the spatial profile of the temperature. The model could also be reformulated to be used in hydrodynamics codes, analogous to the P-α model. This would have the advantage of using the solid density EOS, which is typically better studied. The challenge for this reformulation is that unlike the P-α model, this model would not only involve the thermodynamic conditions of the pore of interest, but also to the other areas of the system, such as the shock, that is contributing to the heating.

BIBLIOGRAPHY

BIBLIOGRAPHY

[1] Y. Aglitskiy, A. Velikovich, M. Karasik, A. Schmitt, V. Serlin, J. Weaver, J. Oh, S. Obenschain, and K. Cochrane. Absolute hugoniot measurements for ch foams in the 2–9 mbar range. *Physics of Plasmas*, 25(3):032705, 2018.

[2] M. L. André. The french megajoule laser project (lmj). *Fusion Engineering and Design*, 44(1-4):43–49, 1999.

[3] C. W. Bamforth. Beer: an ancient yet modern biotechnology. *The Chemical Educator*, 5(3):102–112, 2000.

[4] D. Bancroft, E. L. Peterson, and S. Minshall. Polymorphism of iron at high pressure. *Journal of Applied Physics*, 27(3):291–298, 1956.

[5] M. Barrios, K. Fournier, S. Regan, O. Landen, M. May, Y. Opachich, K. Widmann, D. Bradley, and G. Collins. Backlighter development at the national ignition facility (nif): Zinc to zirconium. *High Energy Density Physics*, 9(3):626–634, 2013.

[6] P. X. Belancourt, W. Theobald, P. A. Keiter, T. J. Collins, M. J. Bonino, P. M. Kozlowski, S. P. Regan, and R. P. Drake. Demonstration of imaging x-ray thomson scattering on omega ep. *Review of Scientific Instruments*, 87(11):11E550, 2016.

[7] B. Bennett, J. Johnson, G. Kerley, and G. Rood. Recent developments in the sesame equation-of-state library. Technical report, Los Alamos Scientific Lab., N. Mex.(USA), 1978.

[8] R. Betti and O. Hurricane. Inertial-confinement fusion with lasers. *Nature Physics*, 12(5):435, 2016.

[9] S. Bhandarkar, T. Baumann, N. Alfonso, C. Thomas, K. Baker, A. Moore, C. Larson, D. Bennett, J. Sain, and A. Nikroo. Fabrication of low-density foam liners in hohlraums for nif targets. *Fusion Science and Technology*, 73(2):194–209, 2018.

[10] T. Boehly, D. Brown, R. Craxton, R. Keck, J. Knauer, J. Kelly, T. Kessler, S. Kumpan, S. Loucks, S. Letzring, et al. Initial performance results of the omega laser system. *Optics communications*, 133(1-6):495–506, 1997.

[11] P. Bridgman. Effects of high shearing stress combined with high hydrostatic pressure. *Physical Review*, 48(10):825, 1935.

[12] D. Britt, D. Yeomans, K. Housen, and G. Consolmagno. Asteroid density, porosity, and structure. *Asteroids III*, pages 485–500, 2002.

[13] M. B. Bryning, D. E. Milkie, M. F. Islam, L. A. Hough, J. M. Kikkawa, and A. G. Yodh. Carbon nanotube aerogels. *Advanced Materials*, 19(5):661–664, 2007.

[14] B. Butcher, M. Carroll, and A. Holt. Shock-wave compaction of porous aluminum. *Journal of Applied Physics*, 45(9):3864–3875, 1974.

[15] E. Campbell, V. Goncharov, T. Sangster, S. Regan, P. Radha, R. Betti, J. Myatt, D. Froula, M. Rosenberg, I. Igumenshchev, et al. Laser-direct-drive program: Promise, challenge, and path forward. *Matter and Radiation at Extremes*, 2(2):37, 2018.

[16] M. Carroll and A. Holt. Static and dynamic pore-collapse relations for ductile porous materials. *Journal of Applied Physics*, 43(4):1626–1636, 1972.

[17] P. Celliers, G. Collins, L. Da Silva, D. Gold, and R. Cauble. Accurate measurement of laser-driven shock trajectories with velocity interferometry. *Applied Physics Letters*, 73(10):1320–1322, 1998.

[18] J. Chihara. Difference in x-ray scattering between metallic and non-metallic liquids due to conduction electrons. *Journal of Physics F: Metal Physics*, 17(2):295, 1987.

[19] J. Chihara. Interaction of photons with plasmas and liquid metals - photoabsorption and scattering. *Journal of Physics: Condensed Matter*, 12(3):231, 2000.

[20] G. Consolmagno and D. Britt. The density and porosity of meteorites from the vatican collection. *Meteoritics & Planetary Science*, 33(6):1231–1241, 1998.

[21] G. B. Cooke. *Cork and the Cork Tree: International Series of Monographs on Pure and Applied Biology: Botany*, volume 4. Elsevier, 2013.

[22] N. R. Council et al. *Review of the Department of Energy's Inertial Confinement Fusion Program: The National Ignition Facility*. National Academies Press, 1997.

[23] J. Delettrez and E. Goldman. Numerical modeling of suprathermal electron transport in laser-produced plasmas. *Laboratory for Laser Energetics, Report*, 36, 1976.

[24] C. Di Stefano, G. Malamud, M. Henry de Frahan, C. Kuranz, A. Shimony, S. Klein, R. Drake, E. Johnsen, D. Shvarts, V. Smalyuk, et al. Observation and modeling of mixing-layer development in high-energy-density, blast-wave-driven shear flow. *Physics of Plasmas*, 21(5):056306, 2014.

[25] R. P. Drake. *High-energy-density physics: foundation of inertial fusion and experimental astrophysics*. Springer, 2018.

[26] D. E. Evans and M. C. Sheehan. Don't be fobbed off: The substance of beer foama review. *Journal of the American Society of Brewing Chemists*, 60(2):47–57, 2002.

[27] K. Falk, C. McCoy, C. L. Fryer, C. W. Greeff, A. L. Hungerford, D. Montgomery, D. W. Schmidt, D. G. Sheppard, J. R. Williams, T. R. Boehly, et al. Temperature measurements of shocked silica aerogel foam. *Physical Review E*, 90(3):033107, 2014.

[28] E. Gamboa, R. Drake, K. Falk, P. Keiter, D. Montgomery, J. Benage, and M. Trantham. Simultaneous measurements of several state variables in shocked carbon by imaging x-ray scattering. *Physics of Plasmas*, 21(4):042701, 2014.

[29] E. Gamboa, C. Huntington, M. Trantham, P. Keiter, R. Drake, D. Montgomery, J. F. Benage, and S. A. Letzring. Imaging x-ray thomson scattering spectrometer design and demonstration. *Review of Scientific Instruments*, 83(10):10E108, 2012.

[30] E. J. Gamboa, D. S. Montgomery, I. M. Hall, and R. P. Drake. Imaging x-ray crystal spectrometer for laser-produced plasmas. *Journal of Instrumentation*, 6(04):P04004, 2011.

[31] R. Gautam, A. Bassi, and E. Yanful. A review of biodegradation of synthetic plastic and foams. *Applied biochemistry and biotechnology*, 141(1):85–108, 2007.

[32] L. J. Gibson. Cork: Structure, properties, applications. *Arnoldia*, 74(1):23–27, 2016.

[33] L. J. Gibson and M. F. Ashby. *Cellular solids: structure and properties*. Cambridge university press, 1999.

[34] S. H. Glenzer and R. Redmer. X-ray thomson scattering in high energy density plasmas. *Rev. Mod. Phys.*, 81:1625–1663, Dec 2009.

[35] G. Gregori, S. H. Glenzer, W. Rozmus, R. W. Lee, and O. L. Landen. Theoretical model of x-ray scattering as a dense matter probe. *Phys. Rev. E*, 67:026412, Feb 2003.

[36] T. C. Hales. A proof of the kepler conjecture. *Annals of mathematics*, pages 1065–1185, 2005.

[37] W. Hansen. Foam-born aphrodite and the mythology of transformation. *The American Journal of Philology*, 121(1):1–19, 2000.

[38] E. Harding, J. Hansen, O. Hurricane, R. Drake, H. Robey, C. Kuranz, B. Remington, M. Bono, M. Grosskopf, and R. Gillespie. Observation of a kelvin-helmholtz instability in a high-energy-density plasma on the omega laser. *Physical review letters*, 103(4):045005, 2009.

[39] C. Haynam, P. Wegner, J. Auerbach, M. Bowers, S. Dixit, G. Erbert, G. Heestand, M. Henesian, M. Hermann, K. Jancaitis, et al. National ignition facility laser performance status. *Applied optics*, 46(16):3276–3303, 2007.

[40] G. Hazak, A. L. Velikovich, J. H. Gardner, and J. P. Dahlburg. Shock propagation in a low-density foam filled with fluid. *Physics of Plasmas*, 5(12):4357–4365, 1998.

[41] W. Herrmann. Constitutive equation for the dynamic compaction of ductile porous materials. *Journal of applied physics*, 40(6):2490–2499, 1969.

[42] R. Hooke. *Micrographia; or, Some physiological descriptions of minute bodies made by magnifying glasses. With observations and inquiries thereupon.* Printed by J. Martyn and J. Allestry, 1665.

[43] K. R. Housen and K. A. Holsapple. Impact cratering on porous asteroids. *Icarus*, 163(1):102–119, 2003.

[44] K. R. Housen, K. A. Holsapple, and M. E. Voss. Compaction as the origin of the unusual craters on the asteroid mathilde. *Nature*, 402(6758):155, 1999.

[45] S. Hu, W. Theobald, P. Radha, J. Peebles, S. Regan, A. Nikroo, M. Bonino, D. Harding, V. Goncharov, N. Petta, et al. Mitigating laser-imprint effects in direct-drive inertial confinement fusion implosions with an above-critical-density foam layer. *Physics of Plasmas*, 25(8):082710, 2018.

[46] J. C. Jamieson, A. Lawson, and N. Nachtrieb. New device for obtaining x-ray diffraction patterns from substances exposed to high pressure. *Review of Scientific instruments*, 30(11):1016–1019, 1959.

[47] A. Jayaraman. Diamond anvil cell and high-pressure physical investigations. *Reviews of Modern Physics*, 55(1):65, 1983.

[48] R. Jeanloz, P. M. Celliers, G. W. Collins, J. H. Eggert, K. K. Lee, R. S. McWilliams, S. Brygoo, and P. Loubeyre. Achieving high-density states through shock-wave loading of precompressed samples. *Proceedings of the National Academy of Sciences*, 104(22):9172–9177, 2007.

[49] E. Jones, T. Oliphant, and P. Peterson. {SciPy}: open source scientific tools for {Python}, 2014.

[50] M. G. Kivelson and C. T. Russell. *Introduction to Space Physics*. Cambridge University Press, 1995.

[51] J. L. Kline, S. Batha, L. Benedetti, D. Bennett, S. Bhandarkar, L. B. Hopkins, J. Biener, M. Biener, R. Bionta, E. Bond, et al. Progress of indirect drive inertial confinement fusion in the united states. *Nuclear Fusion*, 2019.

[52] M. Koenig, A. Benuzzi, F. Philippe, D. Batani, T. Hall, N. Grandjouan, and W. Nazarov. Equation of state data experiments for plastic foams using smoothed laser beams. *Physics of plasmas*, 6(8):3296–3301, 1999.

[53] M. Koenig, A. Benuzzi-Mounaix, D. Batani, T. Hall, and W. Nazarov. Shock velocity and temperature measurements of plastic foams compressed by smoothed laser beams. *Physics of plasmas*, 12(1):012706, 2005.

[54] P. O. Krehl. *History of shock waves, explosions and impact: a chronological and biographical reference*. Springer Science & Business Media, 2008.

[55] C. Kuranz, R. Drake, E. Harding, M. Grosskopf, H. Robey, B. Remington, M. Edwards, A. Miles, T. Perry, B. Blue, et al. Two-dimensional blast-wave-driven rayleigh-taylor instability: experiment and simulation. *The Astrophysical Journal*, 696(1):749, 2009.

[56] A. Latter, R. LeLevier, E. Martinelli, and W. McMillan. A method of concealing underground nuclear explosions. *Journal of Geophysical Research*, 66(3):943–946, 1961.

[57] S. Le Pape, A. Macphee, D. Hey, P. Patel, A. Mackinnon, M. Key, J. Pasley, M. Wei, S. Chen, T. Ma, et al. Density measurement of shock compressed foam using two-dimensional x-ray radiography. *Review of Scientific Instruments*, 79(10):106104, 2008.

[58] S. P. Lyon. Sesame: the los alamos national laboratory equation of state database. *Los Alamos National Laboratory report LA-UR-92-3407*, 1992.

[59] M. MacDonald, P. Keiter, D. Montgomery, H. Scott, M. Biener, J. Fein, K. Fournier, E. Gamboa, G. Kemp, S. Klein, et al. Spatially resolved density and ionization measurements of shocked foams using x-ray fluorescence. *Journal of Applied Physics*, 120(12):125901, 2016.

[60] K. Mahon and T.-W. Lee. Compaction of granular hmx: P-α porosity model in cth hydrocode. *AIP Advances*, 5(12):127121, 2015.

[61] D. L. Matthews, E. Campbell, N. Ceglio, G. Hermes, R. Kauffman, L. Koppel, R. Lee, K. Manes, V. Rupert, V. Slivinsky, et al. Characterization of laser-produced plasma x-ray sources for use in x-ray radiography. *Journal of applied physics*, 54(8):4260–4268, 1983.

[62] D. Maywar, J. Kelly, L. Waxer, S. Morse, I. Begishev, J. Bromage, C. Dorrer, J. Edwards, L. Folnsbee, M. Guardalben, et al. Omega ep high-energy petawatt laser: progress and prospects. *Journal of Physics: Conference Series*, 112(3):032007, 2008.

[63] R. McQueen and S. Marsh. Equation of state for nineteen metallic elements from shock-wave measurements to two megabars. *Journal of Applied Physics*, 31(7):1253–1269, 1960.

[64] N. Meezan, M. Edwards, O. Hurricane, P. Patel, D. Callahan, W. Hsing, R. Town, F. Albert, P. Amendt, L. B. Hopkins, et al. Indirect drive ignition at the national ignition facility. *Plasma Physics and Controlled Fusion*, 59(1):014021, 2016.

[65] E. Mills, P. Wilde, L. Salt, and P. Skeggs. Bubble formation and stabilization in bread dough. *Food and bioproducts processing*, 81(3):189–193, 2003.

[66] K. Nagai, C. S. Musgrave, and W. Nazarov. A review of low density porous materials used in laser plasma experiments. *Physics of Plasmas*, 25(3):030501, 2018.

[67] M. Nelson. *The barbarian's beverage: A history of beer in ancient Europe*. Routledge, 2005.

[68] H. Nishimura, H. Shiraga, H. Azechi, N. Miyanaga, M. Nakai, N. Izumi, M. Nishikino, M. Heya, K. Fujita, Y. Ochi, et al. Indirect-direct hybrid target experiments with the gekko xii laser. *Nuclear Fusion*, 40(3Y):547, 2000.

[69] R. Nora, W. Theobald, R. Betti, F. Marshall, D. Michel, W. Seka, B. Yaakobi, M. Lafon, C. Stoeckl, J. Delettrez, et al. Gigabar spherical shock generation on the omega laser. *Physical review letters*, 114(4):045001, 2015.

[70] R. E. Olson, R. J. Leeper, S. Yi, J. L. Kline, A. Zylstra, R. R. Peterson, R. Shah, T. Braun, J. Biener, B. Kozioziemski, et al. Wetted foam liquid fuel icf target experiments. *Journal of Physics: Conference Series*, 717(1):012042, 2016.

[71] T. Perry and B. Wilde. Nif system-design requirements for nuclear-weapons physics experiments. Technical report, Lawrence Livermore National Lab., CA (United States), 1995.

[72] W. Pincus. Fine Print: Nuclear Program Issues Lead to Congressional Attention. *The Washington Post*, Aug. 2009.

[73] P. M. Platzman and P. A. Wolff. *Waves and interactions in solid state plasmas*. Academic Press, 1973.

[74] C. Ragan III, M. Silbert, and B. Diven. Shock compression of molybdenum to 2.0 tpa by means of a nuclear explosion. *Journal of Applied Physics*, 48(7):2860–2870, 1977.

[75] C. E. Ragan III. Shock compression measurements at 1 to 7 tpa. *Physical Review A*, 25(6):3360, 1982.

[76] S. Regan, V. Goncharov, T. Sangster, E. Campbell, R. Betti, J. Bates, K. Bauer, T. Bernat, S. Bhandarkar, T. Boehly, et al. The national direct-drive inertial confinement fusion program. *Nuclear Fusion*, 59(3):032007, 2018.

[77] B. A. Remington, H.-S. Park, D. T. Casey, R. M. Cavallo, D. S. Clark, C. M. Huntington, C. C. Kuranz, A. R. Miles, S. R. Nagel, K. S. Raman, et al. Rayleigh–taylor instabilities in high-energy density settings on the national ignition facility. *Proceedings of the National Academy of Sciences*, page 201717236, 2018.

[78] C. Rhodes. Lakshmi: Hindu goddess of abundance. *Goddesses in World Culture*, page 1, 2010.

[79] M. Rice, R. G. McQueen, and J. Walsh. Compression of solids by strong shock waves. In *Solid state physics*, volume 6, pages 1–63. Elsevier, 1958.

[80] E. E. Salpeter. Electron density fluctuations in a plasma. *Physical Review*, 120(5):1528, 1960.

[81] H. Sawada, S. P. Regan, D. D. Meyerhofer, I. V. Igumenshchev, V. N. Goncharov, T. R. Boehly, R. Epstein, T. C. Sangster, V. A. Smalyuk, B. Yaakobi, G. Gregori, S. H. Glenzer, and O. L. Landen. Diagnosing direct-drive, shock-heated, and compressed plastic planar foils with noncollective spectrally resolved x-ray scattering. *Phys. Plasmas*, 14(12), 2007.

[82] R. Seebass. Sonic boom theory. *Journal of Aircraft*, 6(3):177–184, 1969.

[83] P. Sterne, L. Benedict, S. Hamel, A. Correa, J. Milovich, M. Marinak, P. Celliers, and D. Fratanduono. Equations of state for ablator materials in inertial confinement fusion simulations. *Journal of Physics: Conference Series*, 717(1):012082, 2016.

[84] H. Sun, Z. Xu, and C. Gao. Multifunctional, ultra-flyweight, synergistically assembled carbon aerogels. *Advanced Materials*, 25(18):2554–2560, 2013.

[85] D. Swift, J. Hawreliak, D. Braun, A. Kritcher, S. Glenzer, G. Collins, S. Rothman, D. Chapman, and S. Rose. Gigabar material properties experiments on nif and omega. *AIP Conference Proceedings*, 1426(1):477–480, 2012.

[86] N. Swisher, C. Kuranz, D. Arnett, O. Hurricane, B. Remington, H. Robey, and S. Abarzhi. Rayleigh-taylor mixing in supernova experiments. *Physics of Plasmas*, 22(10):102707, 2015.

[87] M. B. Syal, D. S. Dearborn, and P. H. Schultz. Limits on the use of nuclear explosives for asteroid deflection. *Acta Astronautica*, 90(1):103–111, 2013.

[88] M. B. Syal, J. M. Owen, and P. L. Miller. Deflection by kinetic impact: Sensitivity to asteroid properties. *Icarus*, 269:50–61, 2016.

[89] R. F. Trunin. Shock compressibility of condensed materials in strong shock waves generated by underground nuclear explosions. *Physics-Uspekhi*, 37(11):1123, 1994.

[90] R. F. Trunin. *Shock compression of condensed materials*. Cambridge university press, 2005.

[91] U.S. Government Accountability Office. Nuclear weapons: Nnsa and dod need to more effectively manage the stockpile life extension program. GAO-09-385, 2009.

[92] R. Vartabedian. Nuclear weapon retrofit falters. *Los Angeles Times*, May 2009.

[93] J. Veverka, P. Thomas, A. Harch, B. Clark, J. Bell, B. Carcich, J. Joseph, C. Chapman, W. Merline, M. Robinson, et al. Near's flyby of 253 mathilde: Images of a c asteroid. *Science*, 278(5346):2109–2114, 1997.

[94] K. J. Walsh. Rubble pile asteroids. *Annual Review of Astronomy and Astrophysics*, 56:593–624, 2018.

[95] W. Wan, G. Malamud, A. Shimony, C. Di Stefano, M. Trantham, S. Klein, D. Shvarts, C. Kuranz, and R. Drake. Observation of single-mode, kelvin-helmholtz instability in a supersonic flow. *Physical review letters*, 115(14):145001, 2015.

[96] S. Wang, P. Austin, and S. Bell. Itsa maze: the pore structure of bread crumbs. *Journal of Cereal Science*, 54(2):203–210, 2011.

[97] T. Watari, M. Nakai, H. Azechi, T. Sakaiya, H. Shiraga, K. Shigemori, S. Fujioka, K. Otani, K. Nagai, A. Sunahara, et al. Rayleigh–taylor instability growth on low-density foam targets. *Physics of Plasmas*, 15(9):092109, 2008.

[98] C. Weir, E. Lippincott, A. Van Valkenburg, and E. Bunting. Infrared studies in the 1-to 15-micron region to 30,000 atmospheres. *J. Res. Natl. Bur. Stand. A*, 63:55–62, 1959.

[99] J. Workman and G. Kyrala. X-ray yield scaling studies performed on the omega laser. *Review of Scientific Instruments*, 72(1):678–681, 2001.

[100] K. Wünsch, J. Vorberger, G. Gregori, and D. O. Gericke. X-ray scattering as a probe for warm dense mixtures and high-pressure miscibility. *EPL (Europhysics Letters)*, 94(2):25001, 2011.

[101] Y. B. ZelDovich and Y. P. Raizer. *Physics of shock waves and high-temperature hydrodynamic phenomena*. Courier Corporation, 2012.

[102] A. Zylstra, S. Yi, B. M. Haines, R. Olson, R. Leeper, T. Braun, J. Biener, J. Kline, S. Batha, L. Berzak Hopkins, et al. Variable convergence liquid layer implosions on the national ignition facility. *Physics of Plasmas*, 25(5):056304, 2018.